CHALMERS
UNIVERSITY OF TECHNOLOGY

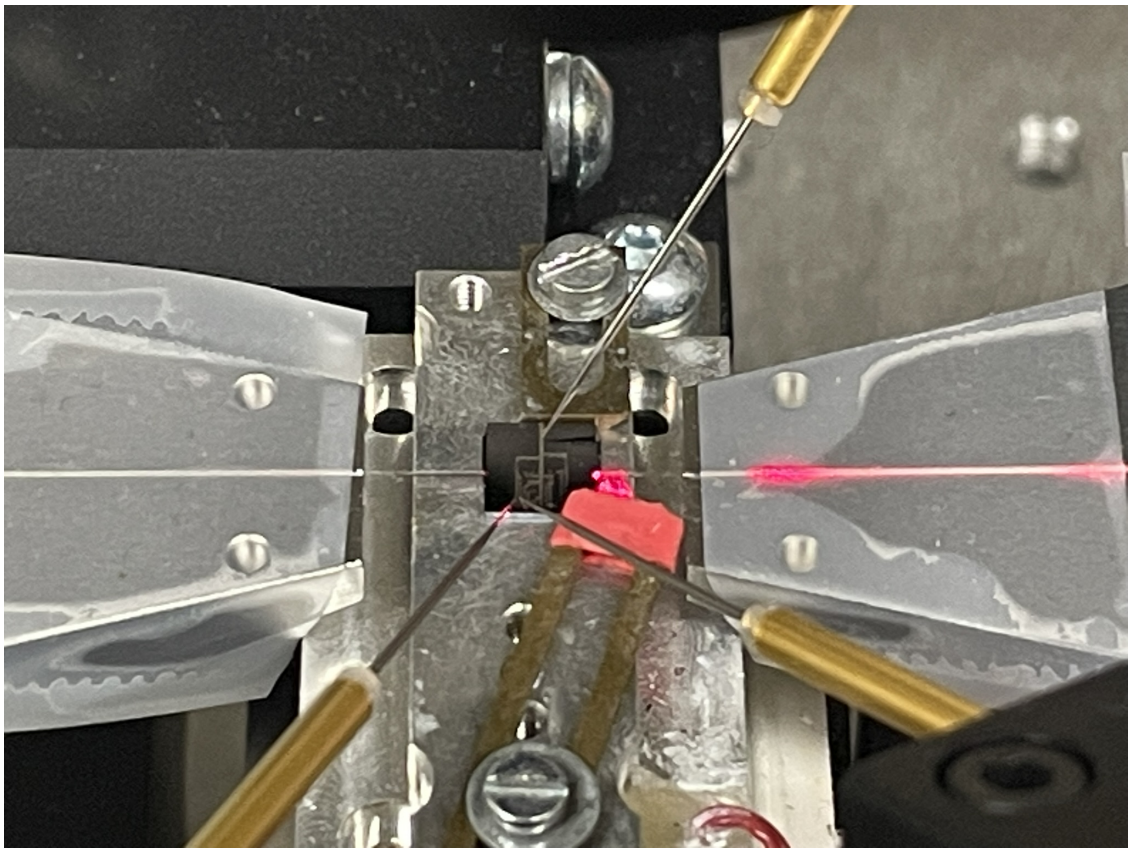

Investigation and Optimization of Photonic Molecule Microcombs with Low Repetition Rates

Master's thesis in Wireless, Photonics and Space Engineering

NORA DZIEIA

DEPARTMENT OF MICROTECHNOLOGY AND NANOSCIENCE (MC2)
CHALMERS UNIVERSITY OF TECHNOLOGY
Gothenburg, Sweden 2025
www.chalmers.se

Master's thesis 2025

Investigation and Optimization of Photonic Molecule Microcombs with Low Repetition Rates

NORA DZIEIA

CHALMERS
UNIVERSITY OF TECHNOLOGY

Department of Microtechnology and Nanoscience (MC2)
Photonics Laboratory
Chalmers University of Technology
Gothenburg, Sweden 2025

Investigation and Optimization of Photonic Molecule Microcombs with Low Repetition Rates
NORA DZIEIA

Supervisor: Carmen Haide López
Examiner: Victor Torres Company

Master's Thesis 2025
Department of Microtechnology and Nanoscience (MC2)
Photonics Laboratory
Chalmers University of Technology
SE-412 96 Gothenburg
Telephone +46 31 772 1000

Cover: Picture of a photonic chip in the optical setup for frequency comb generation that is connected to a laser in the visible range.

Typeset in LaTeX
Printed by Chalmers Reproservice
Gothenburg, Sweden 2025

Investigation and Optimization of Photonic Molecule Microcombs with Low Repetition Rates
NORA DZIEIA
Department of Microtechnology and Nanoscience (MC2)
Chalmers University of Technology

Abstract

Frequency combs are a key technology for many applications, such as optical clocks, precision spectroscopy, and wavelength division multiplexing (WDM) in optical communications. Integrated frequency combs leveraging the Kerr nonlinearity can operate with milliwatt-level pump powers, though their conversion efficiency (CE) typically remains below 10%. In recent years, photonic molecules have been introduced to overcome the problem of generally low CE observed in microcombs. Reported efficiencies have exceeded 50% by transitioning from single cavities to photonic molecule configurations. To date, these levels of CE have only been demonstrated for microresonators with an FSR of 100 GHz. For low FSR photonic molecules, this improvement is challenging due to higher intrinsic losses and a power distribution across a larger cavity volume. In this thesis, we used Ikeda map-based simulations to identify critical design parameters for achieving higher CE in low FSR configurations. We characterized existing chips and compared measured comb spectra with simulations to extract key parameters and quantify the currently achievable CE for different FSRs. This data was used to analyze the influence of multiple parameters on the CE, including coupling factors, input power, and comb detuning. Based on these investigations, we developed improved parameter sets for microresonators with repetition rates of 25 GHz and 50 GHz. The simulated CE increased from 25% (simulation of existing devices) to over 45% for the 25 GHz design. For the 50 GHz design, we present a parameter set that achieves a CE of over 65%. These CE values can be achieved over a range of commonly used input powers in the milliwatt regime. Our results demonstrate the potential to design photonic molecules with tailored FSRs, enabling greater flexibility across applications.

Acknowledgements

I want to take a few words to thank the people who supported me during this thesis work. First, Prof. Victor Torres-Company, who introduced me to the topic of Integrated Photonics and gave me the opportunity to do my thesis in his group. The supervision was truly excellent and our meetings every few weeks gave me guidance on which direction to think in or which question to pursue next.
Next, I would like to thank my supervisor, Carmen Haide López, who was always the first person I turned to when I didn't understand something. She taught me everything I know about photonic microcombs and spent a lot of hours in the lab with me.
I would also like to thank everyone else at the Ultrafast Photonics Laboratory. They welcomed me into their group and were always open to discussing any questions that came up.
During my time at MC2, several other master's students were writing their theses at the same time. I really appreciated our lunch and coffee breaks together, which helped me recharge my batteries and return to my work feeling motivated.
I would also like to thank my family and friends in Germany for supporting me during my two-year master's degree in Sweden. And finally, I would like to thank my partner, Johannes, who patiently listened to all the problems that came up during this work and spent hours discussing them with me.

List of Acronyms

Below is the list of acronyms that have been used throughout this thesis listed in alphabetical order:

CC	Coupled Cavity
CE	Conversion Efficiency
CMOS	Complementary Metal-Oxide-Semiconductor
CW	Continuous Wave
DKS	Dissipative Kerr Soliton
ebeam	Electron-beam
FSR	Free Spectral Range
FWM	Four-Wave Mixing
GVD	Group Velocity Dispersion
HOM	Higher Order Mode
LLE	Lugiato-Lefever Equation
LPCVD	Low-Pressure Chemical Vapor Deposition
MI	Modulation Instability
NLSE	Nonlinear Schrödinger Equation
OSA	Optical Spectrum Analyzer
PM	Powermeter
Q	Quality Factor
SP	Shifted Pump
SWI	Swept Wavelength Interferometry
VOA	Variable Optical Attenuator
WDM	Wavelength Division Multiplexing

Contents

1
Introduction

Integrated silicon nitride microresonators enable compact and cost-effective frequency comb generation, expanding the possible applications across a wider range of fields [1]. These advantages are primarily enabled by the compatibility with CMOS fabrication processes. Silicon nitride, as a platform, offers a relatively high third-order nonlinearity and therefore, enables efficient four-wave mixing (FWM). Additionally, it features low optical losses, which support the realization of high-Q resonators [2].
Microring-based frequency combs are used in applications ranging from optical clocks [3] and LIDAR [4] to communication systems [5], frequency synthesis [6] and spectroscopy [7]. Each of these applications requires a specific FSR to meet its technical requirements. In this thesis, we focus on low-FSR microresonators ($< 50\,\mathrm{GHz}$), which are particularly important for parallelization in communication systems and for frequency synthesis. Given the current limitations in microwave bandwidth, there is a need for photonic solutions that bridge the gap between the microwave and optical domain. In the context of massively integrated parallel WDM, a low frequency spacing between the comb lines is desirable to fully exploit the available communication bands. Additional requirements for parallel WDM systems are high power per comb line and high CE from the pump power into the comb lines.

In recent years, so-called photonic molecules have been presented as a solution to enhance the CE of microring frequency combs from below 10% to above 50% CE in measurements [8]. The fundamental principle of photonic molecules is similar to standard microrings. By accumulating power in the cavity, the nonlinear effect of FWM is initiated and new frequencies are generated. When achieving a balance between gain and loss, as well as the pulse distortion of the Kerr effect and the dispersion, a dissipative Kerr soliton (DKS) will form. The increase in CE is achieved by adding an auxiliary ring to the microresonator system and making use of the mode splitting that occurs from the coupled rings. This overcomes the red detuning requirement of the pump laser and enables frequency matching between the pump laser and the resonance frequency of the microresonator, resulting in a significant increase in CE. To date, conversion efficiencies of 50% have only been demonstrated for microresonators with an FSR of 100 GHz. This thesis aims to evaluate several existing photonic molecule designs, identify potential limitations and develop a 25 GHz design with high CE.
Designing low FSR photonic molecules comes with two fundamental challenges. First, the increased length of the resonator results in higher roundtrip losses, assuming a constant loss factor. Second, the larger cavity volume complicates the

accumulation of sufficiently high intracavity power, which initiates the nonlinear effect of FWM.

During this thesis work, we started by characterizing existing chip designs in the linear regime. This allows for the extraction of key design parameters, namely the coupling strength between the bus waveguide and main ring, and between the main and auxiliary ring. The nonlinear characterization, which investigates the generation of frequency combs, is used to determine the comb spectrum and current CE limits. With these parameters, the chips are simulated, using a Matlab code employing the Ikeda Map and Split-step Fourier Method [9]. Two different models are used for the simulations: a simplified shifted-pump model and a full system model, called the coupled cavity model and capable of predicting detailed comb spectra. By comparing the simulation results, the capabilities and limitations of each model are assessed. Additionally, simulations were carried out to improve our understanding of the dependencies between the chip and simulation parameters on the resulting CE. Parameters that are investigated are the coupling strength between the rings, input power, detuning, and extrinsic and intrinsic Q. Based on these results a new designs for 25 GHz and 50 GHz FSR are developed. For a comprehensive analysis, the new designs are also evaluated in their scalability with respect to input power, intrinsic Q and FSR.

2

Theory

The theory chapter intends first to provide an overview of microresonators in the linear regime and introduce key concepts that are utilized for the soliton generation [10]. Next, the soliton generation process in a single cavity resonator is outlined, along with the most important equations used to model and simulate the phenomenon. Expanding on these fundamental concepts, double cavity microresonators, also called photonic molecules, are introduced as an approach to enhance the CE of DKSs. The critical concept of avoided mode crossings is explained, as it is the underlying physical mechanism enabling the CE improvement in photonic molecules.

2.1 Microresonators

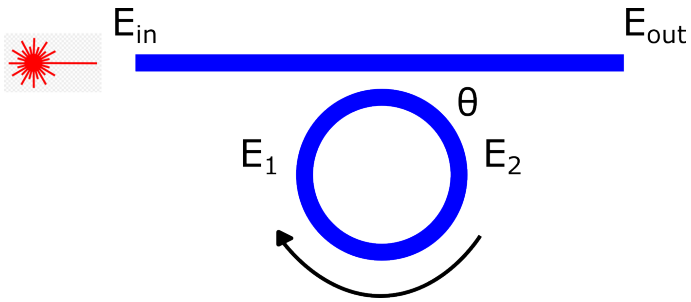

Figure 2.1: Schematic of a ring resonator coupled to a bus waveguide.

A microresonator in its simplest form is a waveguide ring structure that is coupled to a bus waveguide, which provides the input and output ports. For a structure as in Fig. 2.1, the coupling relation between electric fields can be modeled as a point coupler with

$$\begin{bmatrix} E_{\text{out}} \\ E_2 \end{bmatrix} = \begin{bmatrix} \sqrt{1-\theta} & i\sqrt{\theta} \\ i\sqrt{\theta} & \sqrt{1-\theta} \end{bmatrix} \begin{bmatrix} E_{\text{in}} \\ E_1 \end{bmatrix} , \tag{2.1}$$

where θ is the power coupling ratio between the bus waveguide and the resonance. Let E denote the normalized optical fields, such that $P = |E|^2$ holds. The input and output fields from the bus are represented by E_{in} and E_{out}. The fields E_1 and E_2 correspond to the fields immediately before and after the coupling region and, after and before the roundtrip propagation, respectively.

The field evolution during propagation through the waveguide between coupling sections is described in the linear regime by

$$\frac{\partial E}{\partial z} = -\frac{\alpha}{2}E + i\beta(\Delta\omega)E \ , \tag{2.2}$$

where z is the propagation direction and α denotes the loss constant of the waveguide. The propagation constant $\beta(\Delta\omega)$ includes the phase and group velocity, the group velocity dispersion (GVD) coefficient, and higher-order dispersion effects. Solving the differential equation, Eq. 2.2 yields in the field evolution over one round trip with

$$E_1 = E_2 \exp\left(-\frac{\alpha}{2} + i\beta(\Delta\omega)L\right) \ . \tag{2.3}$$

Combining the roundtrip propagation (Eq. 2.3) and the coupling condition between bus waveguide and ring, the transmission spectrum of the microring is given by [10, 11]

$$T = \left|\frac{E_{\text{out}}}{E_{\text{in}}}\right|^2 = \left|e^{i(\pi+\phi)}\frac{a - te^{-i\phi}}{1 - tae^{i\phi}}\right|^2 \ . \tag{2.4}$$

Here, the phase accumulated during a single roundtrip is given by $\Phi = \beta L$ and the field amplitude a decays exponentially as $a = e^{-\alpha L/2}$. t is the amplitude transmission coefficient.

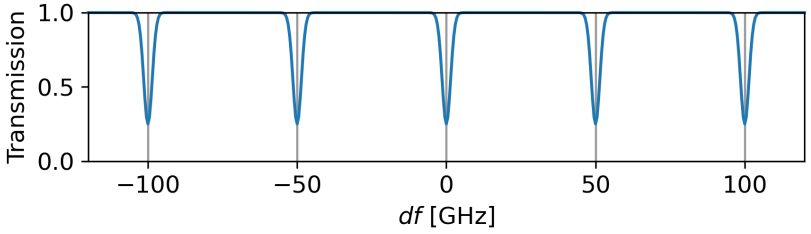

Figure 2.2: Transmission spectrum of a microring resonator with FSR = 100 GHz [10].

Figure 2.2 shows an example transmission spectrum of a microring resonator, including its most significant characteristics. The spacing between the resonances corresponds to the FSR and is defined as

$$\text{FSR} = \frac{c_0}{n_g L} \ . \tag{2.5}$$

The depth of the resonances reflects the loaded quality factor Q of the resonator, a figure of merit that quantifies how many roundtrips the light propagates through the ring before the amplitude is attenuated by a factor of $1/e$. The quality factor can be derived as [10, 12]

$$Q = \frac{\omega_0}{FWHM} = \frac{\omega_0 \mathcal{F}}{FSR} \approx \frac{\omega_0 n_g L\sqrt{ta}}{2(1-ta)c_0} \ , \tag{2.6}$$

with FWHM being the width of the resonance at half maximum. It can also be described using the Finesse $\mathcal{F}$ and the FSR of the resonator. The loaded quality factor can be decomposed into the intrinsic quality factor, which accounts for internal losses α_i, and the extrinsic quality factor, which accounts for coupling-related losses α_c. The relation between the different quality factors is

$$Q^{-1} \approx Q_i^{-1} + Q_e^{-1} \ . \tag{2.7}$$

When $\alpha_{i,c}L \ll 1$, the approxiamtions $a, t \approx 1$ and $1 - \exp\left(-\frac{\alpha_{i,c}L}{2}\right) \approx \frac{\alpha_{i,c}L}{2}$ hold, allowing to relate the loss coefficients to the quality factors by [12]

$$\alpha_i \approx \frac{2\pi n_g}{\lambda_0 Q_i} \ , \qquad \alpha_c \approx \frac{2\pi n_g}{\lambda_0 Q_e} \ . \tag{2.8}$$

For $Q_\mathrm{i} > Q_\mathrm{e}$, the system is considered overcoupled, allowing power to build up in the resonator, which is essential for initiating FWM and the formation of solitons. If $Q_\mathrm{i} < Q_\mathrm{e}$ the system is undercoupled and for $Q_\mathrm{i} = Q_\mathrm{e}$ it is critically coupled. The extrinsic quality and the coupling loss factor are directly linked to the power coupling coefficient θ with

$$\theta = 1 - \exp(-\alpha_c L) \ . \tag{2.9}$$

2.2 Dispersion in Microresonators

Microresonator modes experience two main types of dispersion: material and geometrical dispersion. Material dispersion arises from the inherent frequency dependence of the refractive index $n(\omega)$. For a pulse consisting of different frequency components, defined through the linewidth $\Delta\lambda$, this results in a slightly different refractive index n_g for each frequency within the pulse. The second type of dispersion, geometrical dispersion, results from the confinement strength of the mode within the core, in contrast to the part of the wave that propagates in the cladding. As a result, different parts of the mode experience different refractive indices. The spatial and frequency-dependent refractive indices result in different group velocities $v_g = c/n_g$ within the pulse, causing a temporal distortion of the pulse described by group velocity dispersion GVD $= \frac{\partial}{\partial\omega}\frac{1}{v_g(\omega)}$ [13].

The overall dispersion effects in a microresonator can be described by a Taylor expansion of the propagation constant around a reference frequency ω_ref [10]

$$\beta(\omega - \omega_\mathrm{ref}) = \beta_0 + \frac{\beta_1}{1!}(\omega - \omega_\mathrm{ref}) + \frac{\beta_2}{2!}(\omega - \omega_\mathrm{ref})^2 + \cdots = \frac{2\pi\mu}{L}, \quad (3.12) \tag{2.10}$$

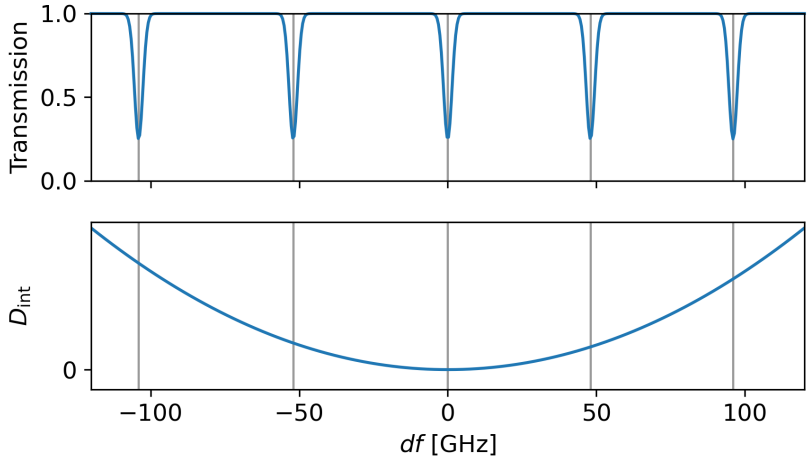

Figure 2.3: Exemplary transmission spectrum of a microresonator with FSR = 50 GHz with anomalous dispersion and the corresponding dispersion D coefficient > 0 (adapted from [10]).

where $\beta_0 = (2\pi n + \Phi)/L$ defines the phase accumulation along the propagation, with the total roundtrip phase given by $\beta_0 L$. $\beta_1 = n_g/c$ describes the inverse group velocity and

$$\beta_2 = \frac{1}{c}\left\{2\frac{\partial n(\omega)}{\partial \omega} + \omega\frac{\partial^2 n(\omega)}{\partial \omega^2}\right\}\Bigg|_{\omega=\omega_0} \tag{2.11}$$

is the group velocity dispersion coefficient, describing how the pulse shape changes over time. $n(\omega)$ is the effective refractive index, taking both the material and geometrical dispersion into account. β also includes higher-order dispersion terms such as β_3, β_4,... However, their influence on the field is negligible for our simulations.

For buried strip waveguides, which are used for the microresonators in this thesis, the propagation constant cannot be analytically calculated anymore. Therefore, it has to be numerically determined or measured directly from manufactured samples. A common method to determine the dispersion of microresonators is to analyze the deviation of the FSR over different mode numbers μ [14, 15]

$$\omega_\mu = \omega_0 + D_1\mu + \frac{D_2}{2!}\mu^2 + \cdots \; ; \quad \mu = 1, 2, \ldots \; . \tag{2.12}$$

The different orders of dispersion are related to the group velocity and GVD as

$$D_1 = -\frac{2\pi}{L\beta_1}, \qquad D_2 = -\frac{LD_1^3}{2\pi}\beta_2 \tag{2.13}$$

For the generation of bright DKS, anomalous dispersion is a necessary condition to balance the pulse distortion induced by the Kerr nonlinearity. Respectively, normal dispersion is needed for dark pulses [16]. Fig. 2.3 illustrates the transmission spectrum and dispersion profile of a resonator with anomalous dispersion. Hence the integrated dispersion parameter is $D_{\text{int}} = \omega_\mu - (\omega_0 + D_1) > 0$ ($\beta_2 < 0$) and $D_{\text{int}} = 0$

at $\mu = 0$. For normal dispersion, $D < 0$ ($\beta_2 > 0$) holds. This dispersion regime is achieved through dispersion engineering, which involves tailoring the cross section of the waveguide such that the combination of material and geometrical dispersion results in an anomalous dispersion profile.

2.3 Frequency Comb and Soliton Generation in Microresonators

For the generation of frequency combs in microresonators, a sequence of physical steps must be performed and controlled by adjusting several system parameters to reach the regime in which DKS exist. In this section, we will focus on so-called bright solitons, which are solitons where localized intensity peaks form within the resonator. This type of soliton requires anomalous dispersion to form. In contrast, dark solitons feature a constant high CW intensity in the resonator with an intensity dip as a soliton. The soliton generation process is initiated by locating the pump laser frequency on the blue side of the resonance ($\omega_\mathrm{p} > \omega_\mathrm{res}$) and then moving it towards the resonance. If the laser frequency approaches the resonance frequency and the system is overcoupled, power builds up in the microresonator. Once the power in the microresonator reaches a threshold power P_th, the Kerr effect initiates four-wave mixing (FWM), generating new frequency lines within the gain region. These initial states are called Modulation Instability (MI) combs. These newly generated comb lines also experience Kerr nonlinearity, leading to the formation of subcombs (Step 1).
The ongoing FWM generates additional frequencies, resulting in a chaotic comb (Step 2). The Kerr effect, combined with increasing temperature resulting from high intracavity power, leads to a redshift of the resonance. To maintain efficient coupling, the laser must be red-detuned relative to the cold-cavity resonance ($\omega_\mathrm{p} < \omega_\mathrm{res}$). The detuning is defined as $\delta_0 = (\omega_\mathrm{res} - \omega_\mathrm{pump})t_R$. With increasing detuning, the system enters a regime where the Kerr-induced spectral broadening and anomalous dispersion compressing of the pulse are in balance, forming dissipative Kerr solitons (DKS) (Step 3) Further increasing the detuning together with a decreasing intracavity power leads to an energy loss of the solitons. This results in a reduction in the number of solitons, since less solitons can be sustained in the system. The remaining solitons will have a higher peak power (Step 4). Eventually, the system reaches a state where only a single soliton remains. This soliton self-stabilizes due to the thermal shift introduced by the soliton power and the red-detuned pump laser. In theory, this soliton is stable over time. However, real-word perturbations, such as a drift in pump frequency and mechanical vibrations, can destabilize the system, resulting in the collapse of the soliton after multiple hours (Step 5) [17, 18].

2.3.1 Mathematical description

The mathematical modeling of dissipative Kerr solitons (DKS) in microresonators relies primarily on two key equations, which together form the Ikeda map. The first equation is the Nonlinear Schrödinger Equation (NLSE). We assume a single-mode

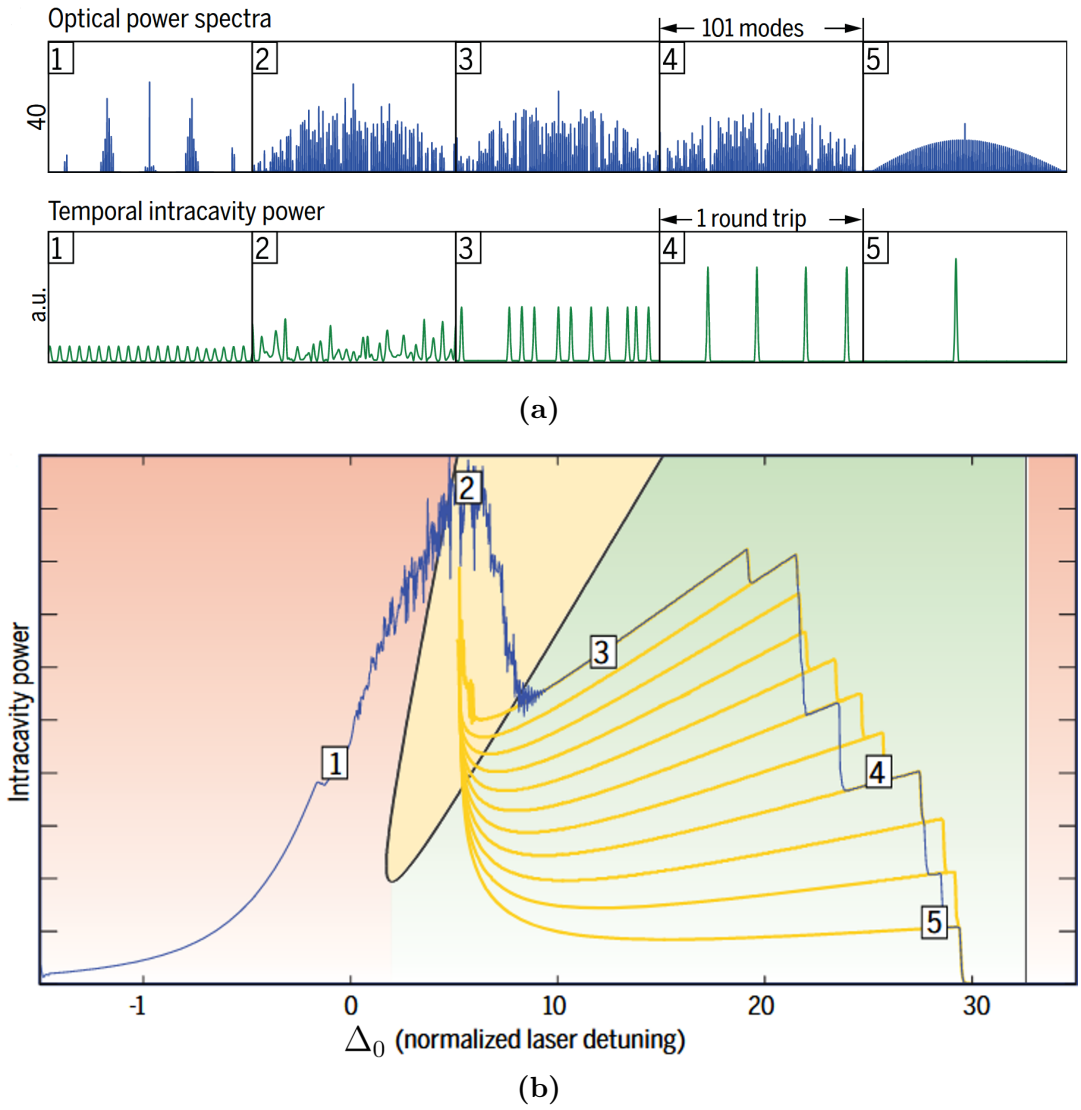

Figure 2.4: Simulated laser scan from the blue-detuned to the red-detuned side of the resonance. (a) showing the average intracavity power evolution during the comb generation process. The blue line is the power evolution of the simulation, the yellow lines show the possible soliton states that could be entered during the scan. The red area indicates where solitons cannot exist. Breathers exist in the yellow area and DKS can exist in the green area. (b) depicts the optical power spectra and the temporal intracavity power at specific points during the scan (reproduced with permission from [17]).

waveguide and neglect polarization effects. This is a fair assumption, as buried waveguides have a preferred polarization mode, and cross-polarizations are filtered out before coupling the light into the chip. In this form, the NLSE is given by [19]

$$\frac{\partial E(z,\tau)}{\partial z} = -\frac{\alpha_i}{2}E - i\frac{\beta_2}{2}\frac{\partial^2 E}{\partial \tau^2} + i\gamma|E|^2 E, \tag{2.14}$$

and describes the electric field traveling through the microresonator (z) and how the

pulse evolves over time ($\tau = t - z/v_g$). Eq. 2.14 extends the linear form of Eq. 2.3 by including nonlinear effects. The NLSE accounts for internal losses α_i, group velocity dispersion β_2 and the Kerr-nonlinearity γ, obtained as

$$\gamma = n_2 \frac{\omega_0}{c A_{\text{eff}}} \tag{2.15}$$

n_2 being the nonlinear refractive index coefficient, ω_0 being the pump frequency, c being the speed of light in vacuum and A_{eff} being the effective area of the mode in the waveguide.

The second key equation describes the coupling between the bus waveguide and the microresonator using Coupled Mode Theory. The field after the coupling process, and before the next roundtrip is defined as

$$E^{(m+1)}(z=0,\tau) = \sqrt{\theta} E_{\text{in}} + \sqrt{1-\theta} E^{(m)}(z=L,\tau) e^{i\phi_0}, \tag{2.16}$$

E_{in} being the input electric field, $E^{(m)}$ being the field at the end of the m-th roundtrip and $E^{(m+1)}$ the field after coupling, but before the next roundtrip. Additionally, the phase accumulated during the roundtrip compared to the pump field is accounted for by Φ_0.

Using Eq. 2.3 and Eq. 2.16, the full system dynamics of a microresonator pumped with a CW laser can be described. Together these equations form the so-called Ikeda map, which serves as the foundation for the mathematical modeling of the fields in the simulation code. A more detailed description of the modeling is provided in Section 3.3. For a high Q resonator, implying low internal losses and low coupling losses per round trip ($\alpha_i L, \theta \ll 1$), the field changes over one roundtrip become negligible. Under this assumption, the Ikeda map equations can be combined into a partial differential equation. This equation is known as the driven damped NLSE or Lugiato-Lefever equation (LLE), named after Lugiato and Lefever, who introduced the equation for soliton modeling in cavities [20]. The combined equation is given by [16]

$$t_R \frac{\partial E(t,\tau)}{\partial t} = \underbrace{-\alpha}_{\text{Loss}} \underbrace{- i\delta_0}_{\text{Detuning}} \underbrace{- iL\tfrac{\beta_2}{2}\tfrac{\partial^2}{\partial \tau^2}}_{\text{Dispersion}} \underbrace{+ i\gamma L |E|^2}_{\text{Kerr effect}} E + \underbrace{\sqrt{\theta} E_{\text{in}}}_{\text{Coupling}}. \tag{2.17}$$

Variations within each roundtrip are captured using the fast varying time variable τ and the field evolution over several round-trips is described using the slow varying time variable t. t_R is the roundtrip time and the loss factor α defines the total roundtrip loss, including internal losses and coupling losses with $\alpha = (\alpha_i L + \theta)/2$. δ_0 is the phase that the light in the cavity accumulates per roundtrip in reference to the pump laser, defined as $\delta_0 = 2\pi l - \Phi_0$ [rad]. The detuning is equivalent to the detuning defined in Section 2.3.

The LLE, Eq. 2.17, is commonly used in its normalized form

$$\frac{\partial E(t,\tau)}{\partial t} = \left[-1 + i(|E|^2 - \Delta) - i\eta \frac{\partial^2}{\partial \tau^2} \right] E + S. \tag{2.18}$$

To obtain the normalized LLE, the following normalizations are applied:

- $t \rightarrow \alpha t/t_R$
- $\tau \rightarrow \tau\sqrt{\frac{2\alpha}{|\beta_2|L}}$
- $E \rightarrow E\sqrt{\frac{\gamma L}{\alpha}}$

The normalized pump strength is given by $S = E_{in}(\gamma L\Theta/a^3)^{1/2}$ and the normalized detuning is given by $\Delta = \delta_0/\alpha$. η defines the type of dispersion, with -1 being anomalous dispersion, needed for bright solitons.

For the simplest steady-state solution of the LLE with a homogeneous field, hence $\partial E/\partial\tau, t = 0$, the so-called cubic equation of optical bistability can be derived [21]:

$$X = Y^3 - 2\Delta Y^2 + (\Delta^2 + 1)Y, \tag{2.19}$$

with $X = |S^2|$ and $Y = |E|^2$. It can describe the intracavity power depending on the detuning Δ and the input power S. From the bistability equation or the corresponding curve (Fig. 2.5) the threshold power

$$P_{th} = \frac{\alpha}{\gamma L} \tag{2.20}$$

that has to be achieved in the cavity to initiate Modulation Instability (MI) can be derived [10]. This threshold represents the minimum intracavity power required for the parametric gain to exceed the cavity losses, allowing newly generated frequencies within the gain bandwidth to be sustained. This starts the FWM process and initiates the DKS comb generation. The bistability curve itself illustrates the shift of the resonance for a given nonlinear coefficient γ with increased detuning. Additionally, it demonstrates the necessity of approaching the DKS regime from the blue-detuned side, allowing the system to evolve on the stable branch (solid line) of the curve. The dashed line is the unstable branch, which represents a non-physical state.

2.4 Coupled Cavity or Photonic Molecule

In recent years, the photonic molecule has been presented as an adapted version of the microring resonator, enabling much higher CE. These photonic molecules consist of a main ring with the same dimensions as the corresponding single cavity layout, and a second much smaller ring, as depicted in Fig. 2.6. This additional ring is called auxiliary ring. By locating the auxiliary ring in close proximity to the main ring, the modes in both systems interact, resulting in a shared transmission spectrum. This interaction is described by the coupled-mode theory. When the resonance of the main ring and the auxiliary ring are close in frequency, avoided mode crossing occurs, resulting in two new resonances defined by the eigenvalues of the system. This resonance splitting is similar to the state splitting in diatomic molecules. Hence the name photonic molecules. These split resonances enable operating the laser

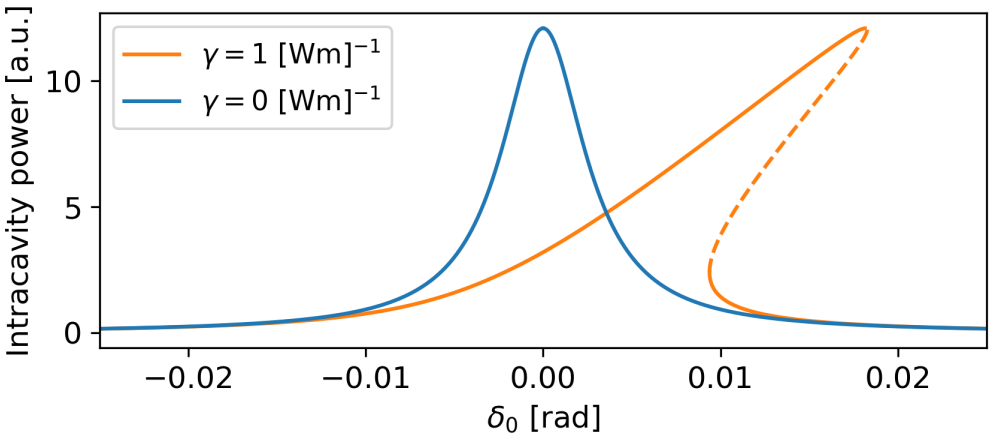

Figure 2.5: Exemplary bistability curve illustrating the intracavity power and the resonance shift introduced by the Kerr effect, whose strength is given by the nonlinearity coefficient γ (adapted from [10]).

in the center of the red-shifted resonance, while the comb frequencies themselves still fulfill the condition of being red-detuned in reference to the cold non-coupled resonance [9]. In the following section, the system of photonic molecules will be discussed in greater detail.

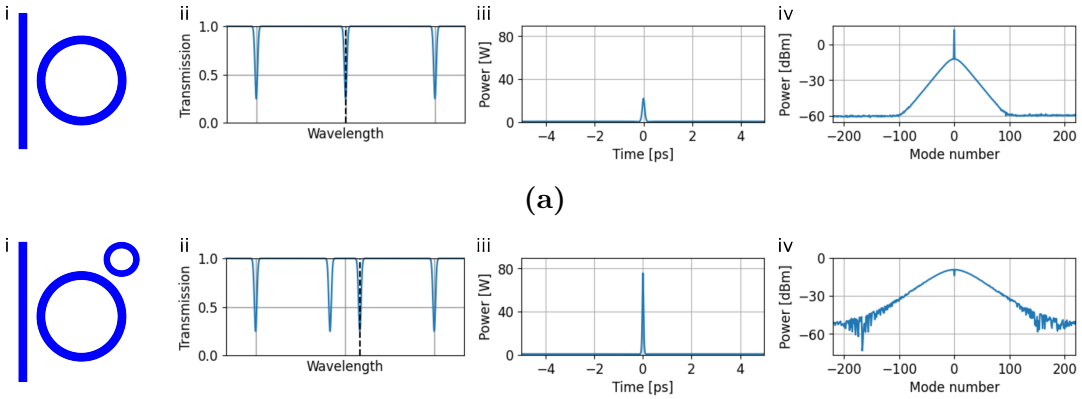

(a)

(b)

Figure 2.6: Comparison between a single cavity microresonator (a) and a coupled cavity microresonator (b). i. shows the schematic of the microresonators, ii. the transmission spectrum with the pump location indicated by the dashed line, iii. the soliton in the time domain in the ring and iv. the resulting comb spectrum with the pump line in the center (adapted from [22]).

2.4.1 Avoided mode crossings

By putting the two rings in close proximity to each other the modes in the resonators interact and coupled-mode theory has to be applied to describe the system. Due

to avoided mode crossing, the resonance will split if the main and the auxiliary resonance are close in frequency. These resonance locations, so called supermodes, are the eigenfrequencies of the new combined system and given by [9]

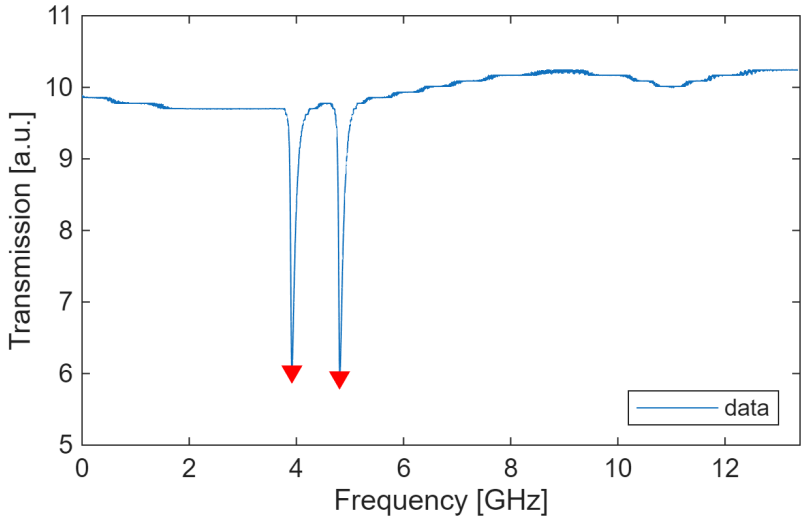

Figure 2.7: Measured transmission spectrum of a photonic molecule with FSR = 25 GHz and a minimal resonance distance of $2\kappa/2\pi = 0.89$ GHz.

$$\omega^{(s,a)} = \frac{\omega_{\text{main}} + \omega_{\text{aux}}}{2} \pm \left[\frac{(\omega_{\text{main}} - \omega_{\text{aux}})^2}{4} + |\kappa|^2 \right]^{1/2} , \tag{2.21}$$

where κ is the coupling coefficient between the main and the auxiliary ring. If $\omega_{\text{main}} = \omega_{\text{aux}}$ the equation can be simplified to

$$\omega^{(s,a)} = \omega_{\text{main,aux}} \pm \kappa , \tag{2.22}$$

with $\delta f = 2\kappa/2\pi$ denoting the closest frequency separation between the resonances. The mode crossing causes a transmission spectrum such as in Fig. 2.7. The coupling strength between the rings is also often described by the power coupling coefficient, which is given by

$$\theta_c = \left(\frac{2\pi\delta f}{\text{FSR}_{\text{main}}} \right)^2 . \tag{2.23}$$

2.4.2 DKS in Photonic Molecules

The dynamics of a photonic molecule can be described using an adapted form of the equations used for the single cavity system. Unlike in the single cavity system, the field in the auxiliary ring must also be modeled, and the coupling between the rings must be taken into account. This set of equations describes the field evolution in the main ring as A_1 and in the auxiliary ring as A_2 [10]

$$\frac{\partial A_1}{\partial z} = \left(-\frac{\alpha_1}{L} - i\frac{\delta_1}{L} - i\frac{\beta_2^{(\text{main})}}{2}\frac{\partial^2}{\partial t^2} - i\gamma_1|A_1|^2 \right) A_1 + i\kappa_z A_2 + i\frac{\sqrt{\theta}A_{\text{in}}}{L} \tag{2.24}$$

$$\frac{\partial A_2}{\partial z} = \left(-\frac{\alpha_2}{L} - i\frac{\delta_2}{L} - d\frac{\partial}{\partial t} - i\frac{\beta_2^{(\text{aux})}}{2}\frac{\partial^2}{\partial t^2} - i\gamma_2|A_2|^2 \right) A_2 + i\kappa_z A_1 \ . \tag{2.25}$$

The terms within the parentheses describe the field evolution, governed by the NLSE. The parameter d represents the walk-off factor, indicating the offset in group velocity between the two cavities. The additional terms account for coupling effects, where κ_z defines the coupling strength between the two rings. The units of κ_z are [rad/k], hence it is related to the propagation constant of the two modes. According to [10] $\kappa_z \approx \kappa 2\pi (L D_1^{(\text{main})} D_1^{(\text{aux})})^{-1/2}$. θ characterizes the coupling between the bus waveguide and the main ring.

The photonic molecule configuration enables significantly higher conversion efficiency, defined as

$$\text{CE} = \frac{\sum_i P_{\text{line},i} - P_{\text{line,pump}}}{P_{\text{in,pump}}} \ . \tag{2.26}$$

$P_{\text{line},i}$ is the power of each frequency line in the comb, $P_{\text{line,pump}}$ is the power of the pump line and $P_{\text{in,pump}}$ is the input pump power. The CE serves as a figure-of-merit for how efficiently the pump power is utilized to generate comb lines.
This enhanced CE is achieved by operating the pump laser at the center of the split-resonance, rather than red-detuning it as in the single cavity configuration. This is feasible, since the comb frequencies themselves remain red-detuned relative to the uncoupled resonance location. To ensure that the pump frequency is located in the resonance center, the detuning is defined as half the distance between the resonances $\delta_0 = 2\pi \text{FSR}^{-1} \delta f/2$, as depicted in Fig 2.6 ii.
As a result of matching the pump and the resonance frequency, the intracavity power increases and higher detuning values become accessible. This in turn leads to the generation of a higher number of comb lines [23]. The soliton formed in the photonic molecule exhibits higher peak power, a broader comb shape and a reduced pump line intensity within the spectrum. However, the auxiliary ring leads also to an additional loss factor for the main ring, since the power will distribute over both rings.
An additional advantage of the photonic molecule is a broader existence range of the soliton states, which has been extensively studied in [9, 8]. This wider existence range simplifies the experimental comb generation process. Simulations have shown that the coupling strength between the two rings strongly influences the size of the existence range. Deviations of κ significantly reduce the size of the existence range and shift the existing range to other detuning values.

3
Methods

3.1 Chip Layout

The fabrication process and the waveguide design for microresonator photonic chips in silicon nitride (Si_3N_4) have been extensively investigated and optimized in previous works [24][2]. As a result of these prior developments, the chips characterized in this thesis are based on a Si_3N_4 buried waveguide structure with silicon dioxide (SiO_2) cladding. Si_3N_4 exhibits numerous advantages for nonlinear photonic applications. First, it has a relatively high nonlinear refractive coefficient n_2, enabling FWM. Second, its low material losses, combined with an optimized fabrication technique, allow for microresonators with high Q_i exceeding 10 million. Additionally, the fabrication process allows for standard deposition methods, such as low-pressure chemical vapor deposition (LPCVD), enabling compatibility with CMOS technology and allowing for high-volume and low-cost manufacturing processes [25].
The waveguide cross section has been specifically engineered such that anomalous dispersion is achieved, which is an essential condition for the generation of a bright soliton. The waveguide geometry depicted in Fig. 3.1a yields a GVD of $\beta_2 = -80\,\mathrm{ps}^2/\mathrm{km}$. The waveguide exhibits a refractive group index of around $n_g = 2.1$ and achieves a Q_i of around 10 million. However, microresonators with Q_i values up to 19 million have been demonstrated in [2], using similar geometries.

The basic waveguide fabrication process follows a standard lithographic process. The substrate consists of a thermal wet oxidized SiO_2 substrate. On top of the substrate, a layer of Si_3N_4 is deposited. Subsequently, a photoresist layer is applied and electron-beam (ebeam) lithography is used for a high-precision development of the resist pattern. The final waveguide structure is then etched into the Si_3N_4 layer. Afterwards, the top cladding layer of SiO_2 is applied using chemical vapor deposition to encapsulate the waveguide structure [24].

For this thesis, two different photonic molecule designs with a main ring FSR of 25 GHz and 100 GHz have been characterized. To achieve 25 GHz FSR with the given n_g a radius of approximately 910 µm is required. However, the writing field of the ebeam is too small to develop a circular structure with the specified radius. Therefore, a more space efficient finger-shaped resonator layout is employed, as depicted in Fig. 3.1b. This layout has been specifically designed to overcome the problem of higher order mode (HOM) generation, primarily caused by mode mismatching between the bent and straight waveguide. By employing an adiabatic bent

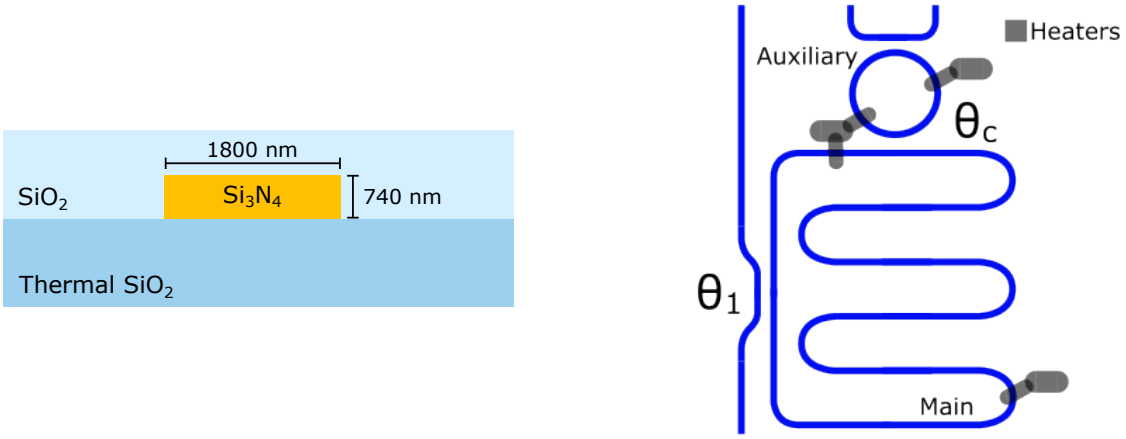

(a) **(b)**

Figure 3.1: Schematic of (a) the cross section waveguide structure and (b) the 25 GHz photonic molecule layout realized in a finger structure to improve space efficiency. The integrated heater pads are used to apply a voltage and thereby enable control over the resonance locations.

geometry, the HOM generation is suppressed, resulting in a single-mode transmission spectrum [2]. For the coupling between the bus waveguide and the main ring, an adiabatic coupler is utilized. This coupler layout provides two degrees of freedom for adjusting the coupling strength: the length of the coupling region and the gap between the waveguides. For the coupling between the main and auxiliary ring, a point coupler is deployed. Hence, only the gap between the waveguides defines the coupling strength. The auxiliary ring is also weakly coupled to a separate bus waveguide, theoretically enabling the possibility to characterize the auxiliary ring parameters. However, the chip stages used in this work, together with the current chip design, do not allow direct characterization of the auxiliary ring. The outputs of the waveguides for the auxiliary ring are located on the same side of the chip, which does not allow both facets to be coupled to the taper fibers due to space constraints. Instead, the Q values of the auxiliary ring are assumed to be similar to the values reported in [9].
The 100 GHz layout follows the same structure as the 25 GHz layout. Although due to a smaller resonator radius of around 228 µm, a simple circular resonator is sufficient. Consequently, both the bus-main and main-auxiliary coupler are implemented as point couplers.

To introduce an additional degree of freedom to the transmission spectrum of the photonic molecule, thermal heaters are added onto the two microresonator rings. By applying a voltage to the heater pads, the temperature of the rings can be manually adjusted, resulting in a redshift of the resonances. This thermal tuning effect is used during the comb generation process in the laboratory to move the auxiliary resonance towards the main ring resonance.

3.2 Measurements

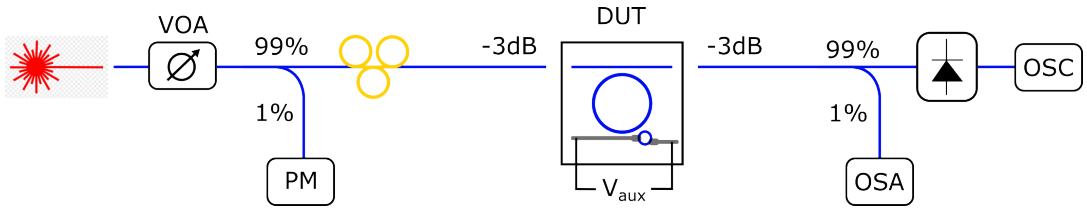

Figure 3.2: Simplified schematic of the measurement setup. The power level of the CW laser source is adjusted using the VOA. The power level is observed by the PM. The polarizer filter is used to filter out the TM mode, leaving only the fundamental TE mode. The chip features heater pads to apply a voltage that controls the position of the resonances. After the chip, the power is measured by a diode that forwards the signal to an oscilloscope. For comb measurements, the optical spectrum analyzer (OSA) is connected.

For both the linear characterization and the comb generation, a similar lab setup is used. A schematic of the setup, including the elements for the comb generation, is depicted in Fig. 3.2. The chip is placed on a stage and coupled to the fiber using tapered fibers, which are placed in close proximity to the chip facets. The coupling losses are approximately 3 dB per facet. The on-chip power can be measured using a powermeter (PM) placed in front of the chip, with the coupling losses accounted for by subtracting the corresponding value from the PM reading. To ensure single-mode operation, a polarization controller is placed in front of the chip.
For the linear characterization, the laser is swept over the relevant frequency range to obtain a full transmission spectrum of the resonances. This process is known as swept wavelength interferometry (SWI) and uses frequency calibration of the resonances in the spectrum. As a reference, we either use a Menlo laser or a Mach-Zehnder interferometer. The SWI process is described in detail in [26]. From the transmission spectrum, the FSR and the GVD can be directly determined. By fitting a Lorentzian function to the resonances, the quality factors Q_i and Q_e can be extracted.

For the comb generation, a similar setup is used as for the linear lab measurements, with additional control mechanisms for the input power, the auxiliary ring resonance location and the pump laser frequency. A variable optical attenuator (VOA) is placed after the laser for the input power control and a voltage is applied to the heater pads on the chip to control the resonance locations.
To generate the comb, the offset between the rings, pump detuning and input power have to be gradually tuned, following a specific path. The process is started by locating the auxiliary ring resonance and the laser frequency on the blue-detuned side of the main resonance. First, we tune the pump frequency toward the resonance until nonlinear effects, such as MI, occur. Next, the voltage V_aux applied to the auxiliary heater pad is gradually increased. This thermal tuning shifts the auxiliary ring resonance towards the main ring resonance, hence generating the mode splitting. During this process, multiple states may be observed on the OSA, from MI combs

over chaotic comb forms and multiple solitons in the cavity. At this point, the laser power is locked to a low power state, resulting in a lower input power. By carefully continuing to increase the auxiliary ring heater voltage, a stable DKS state can be achieved. The CE can then be optimized by further reducing the input power. An in-depth overview of the generation of efficient comb states is presented in [8, 9].

3.3 Simulation Model

All simulations of Kerr frequency combs within this thesis were performed using a custom simulation code based on the work of Óskar Helgason, presented in [8]. The code implements the Ikeda map consisting of two equations: the coupling equation between the bus waveguide and the ring (Eq. 2.16) and the NLSE (Eq. 2.14). The nonlinear differential equations are solved by applying the split-step Fourier method [19], which simulates the field evolution in the cavity over time. Two versions of the code were used to simulate different aspects of the designs: the single-cavity with shifted pump (SP) code and the coupled-cavity (CC) code.

All simulation models start by defining all input parameters, which include: FSR, δ_0, Q_i, Q_e, n_g, P_{in}, GVD β_2, and the nonlinear coefficient γ.
In the single cavity simulations, these input parameters are used to compute an initial steady-state CW solution by finding the roots to the polynomial form of the bistability equation (Eq. 2.19). From this initial solution, the field evolution over multiple roundtrips is simulated using the coupling matrix and split-step Fourier method. The description and simulation of solitons have been extensively studied in [18].

The SP code is a modified version of the single-cavity code, adapted to model specific aspects of photonic molecule behavior. Although the SP code is employed to investigate othe photonic molecule behavior, it takes only a single resonance into account. The influence of the second ring is incorporated by introducing a phase shift to the pump frequency, ensuring frequency matching of the pump into the main resonance. This is achieved by setting the detuning of the pump to zero and applying the detuning shift only to the remaining frequency components of the comb. This model enables the frequency comb to be sustained at higher detuning values, resulting in combs with higher CE. However, it is important to note that the model does not account for the loss introduced by the auxiliary ring, which results in a overestimation of the CE.

To simulate the full dynamics, the CC code is employed, extending the model to include two coupled rings. The adjusted full system equation, combined from the LLE and the coupling matrices between the bus and main ring and between the main ring and auxiliary, is significantly more complex than the single cavity system. Instead of two steady-state solutions, the CC can support up to 9 solutions. Consequently, it is not feasible to determine an initial field. To address this problem, the simulation process is started with the power build-up process in the photonic molecule, following the soliton generation steps discussed in Section 2.3. Therefore,

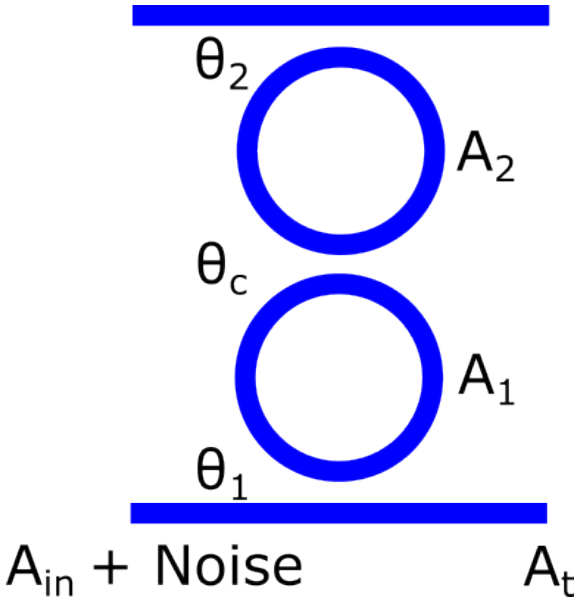

Figure 3.3: Schematic of the ring layout used for the coupled cavity simulations. The system consists of two rings of identical length L. Each ring is coupled to a bus waveguide with the coupling strength defined by the power coupling ratio θ. The CW laser input A_{in}, including noise, is coupled to one side of the waveguide. The output signal at the end of the waveguide is denoted as A_{t}. A_1 and A_2 are the optical fields in ring 1 and ring 2, respectively.

three vectors are defined for P_{in}, δ_0 and the offset between the main and the auxiliary resonance to dynamically adjust the system parameters. The offset vector simulates how the auxiliary resonance is moved towards the main resonance, initiating the split-resonance state. The detuning vector defines the laser position relative to the cold main resonance. Starting with a negative value, it simulates the laser moving into the red-detuned side ($\omega_p > \omega_0$). The power vector is initialized with a high input power to induce gain in the resonator and therefore initiate the FWM process. Subsequently, the power is gradually reduced to reach the regime where stable and efficient solitons exist.

The simulation layout of the photonic molecule is a simplified two-ring structure with equal physical length, as illustrated in Fig. 3.3. However, the FSR of the rings is the actual FSR and therefore includes the size difference of the rings. To accurately reflect the dispersion profile, the refractive index is adjusted to $n_{g,\text{aux}} = c_0/(L_1\text{FSR}_2)$, with L_1 being the physical length of the main ring and FSR_2 being the actual FSR of the auxiliary ring. The number of longitudinal modes in each ring is modified to reflect the number of modes, based on the modulus of the FSRs, specifically $\text{mod}(\text{FSR}_2, \text{FSR}_1)$.

To simulate the field propagation over a roundtrip in the CC model, both the Ikeda map and the split-step Fourier method are employed. First, the main ring length is divided into two segments of size $h = L_1/2$ and the dispersion parameter D is determined from the wave constant. The roundtrip simulation begins with the coupling

Algorithm 1 Coupled Cavity Roundtrip Simulation

$h = L/2$
For $n = 1$ to $N_{\text{roundtrips}}$
$D = i\beta_0 + i\beta_1\omega + \frac{\beta_2}{2}\omega^2$ % define dispersion operator
  Bus - main ring coupling
    $A_{\text{in}} = \sqrt{P_{\text{in}}} + N$
    $A_{\text{t}} = A_{\text{in}}\sqrt{1-\theta_1} + A_1\sqrt{\theta_1}$
    $A_1 \leftarrow A_1\sqrt{1-\theta_1} + A_{\text{in}}\sqrt{\theta_1}$
  Multisteps (A_1)
    $N = i\gamma|A|^2$ % define nonlinear operator
    $A \leftarrow A \cdot e^{hN/2}$ % half nonlinear step
    For $n = 1$ to $N_{\text{steps}} - 1$
      $A \leftarrow \mathcal{F}\left(e^{hD_\omega}\mathcal{F}^{-1}(A)\right)$ % full linear step
      $A \leftarrow A \cdot e^{hN}$ % full nonlinear step
    end
    $A \leftarrow A \cdot e^{hN/2}$ % half nonlinear step
  Multisteps (A_2)
  [...]
  Main - auxiliary ring coupling
    $A_1 \leftarrow A_1\sqrt{1-\theta_c} + A_2\sqrt{\theta_c}$
    $A_2 \leftarrow A_2\sqrt{1-\theta_c} + A_1\sqrt{\theta_c}$
  Multisteps (A_1)
  [...]
  Multisteps (A_2)
  [...]
end

between the bus waveguides and the main and auxiliary ring, respectively. Subsequently, the propagation of the fields over half a roundtrip in each ring is simulated using the Split-step Method. This is implemented by dividing the propagation step into segments of equal size $(h/2)$. In the first segment, the nonlinear effect is applied using the nonlinear operator $N = i\gamma|A|^2$, while $D = 0$. The linear segment applies the dispersion effects by using the dispersion coefficient D, while $N = 0$. This propagation description corresponds to the function referred to as "Multisteps" in Algorithm 1. After simulating half a roundtrip, the coupling between the rings is calculated, defined by the power coupling coefficient θ_c. The Multistep process is then repeated to simulate the second half of the roundtrip propagation. The total number of simulated roundtrips is defined by $N_{\text{roundtrips}}$ [9].

3.3.1 Design Flow

For the simulations in this thesis, both the SP and CC code were used. The optimization process was structured in a certain design flow to reduce simulation time and ensure comparability across designs. Certain parameters, such as Q_{i} and the GVD, are fixed properties of the chip and serve as input chip parameters. Next, the

last chip parameter, the coupling strength between the bus waveguide and the ring, is defined using Q_e. Based on these inputs, all remaining parameters are automatically calculated. Once the chip parameters are set, the simulation parameters P_{in} and δ_0 can be optimized. These are the same parameters used for the experimental comb generation to optimize the CE. In general, higher detuning leads to more comb lines and thus higher CE, while lower P_{in} improves the CE due to a more favorable ratio in the CE definition.

In the SP simulation, the optimization process is straightforward. The chip and the simulation parameters are defined simultaneously and the LLE yields a steady-state solution of the field in the ring. This allows for a direct evaluation of the CE at the given parameters. The detuning is then stepwise increased and the Pin is decreased until the point of maximum CE is found.
In contrast, the CC simulation involves a more complex workflow. First, the chip parameters are defined and then parameter vectors for the offset, the detuning and the input power leading to the final simulation parameters must be found. Since the coupling between the rings is now taken into account, the final detuning value is directly calculated from the coupling coefficient κ. At the final step, P_{in} is reduced to find the maximum CE for the given chip configuration. However, to optimize the detuning, κ must be adjusted. This requires iterating over increasing coupling values and finding a new vector each time, until the maximum detuning and corresponding κ values are identified. Only in the next step the same process is repeated for another Q_e, finding the corresponding P_{in} and detuning value. Once multiple optimized designs are found, a descending optimization path can be identified to find a design that meets a specific target input power.

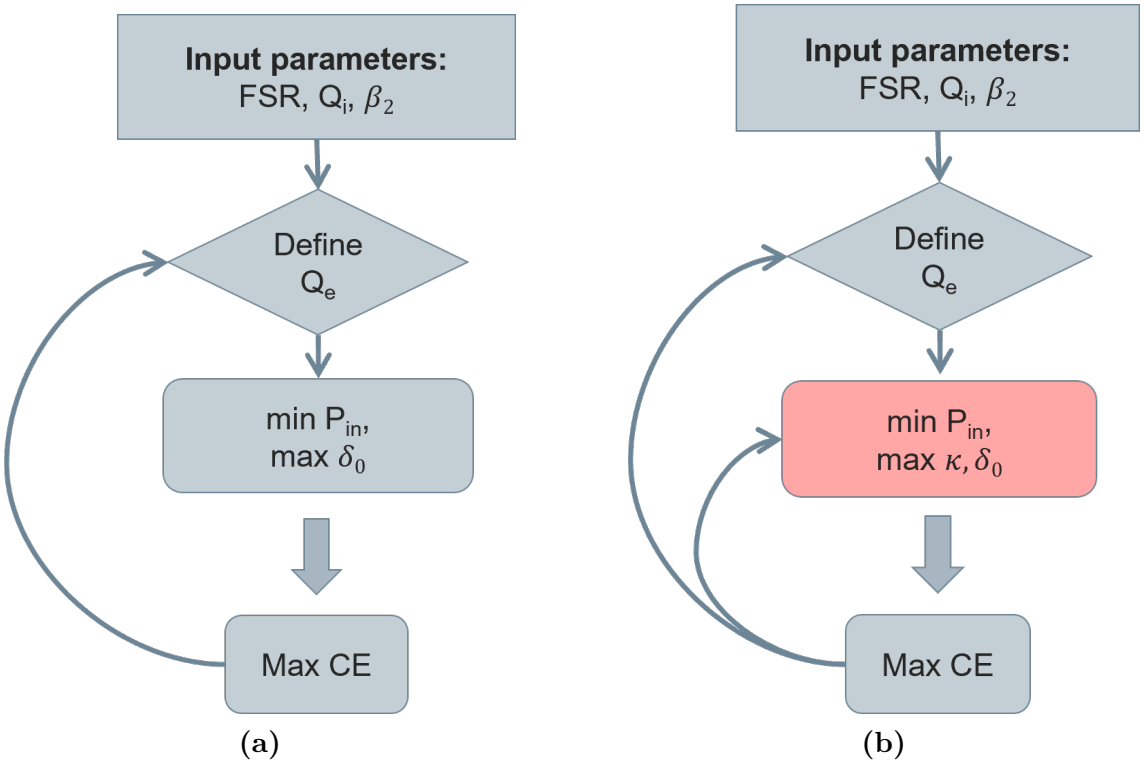

Figure 3.4: Visualization of the optimization process used for the (a) Shifted Pump and (b) for the Coupled Cavity code.

4
Results

This thesis aims to enhance photonic molecule design with a FSR = 25 GHz in terms of CE, building upon an existing chip design from the Ultrafast Photonics group at Chalmers. For chips with an FSR of 100 GHz, CEs exceeding 50% have been demonstrated in both simulations and measurements. In contrast, lower-FSR configurations have not yet achieved comparable performance. As an initial step, various existing chip designs were characterized to extract key parameters, including the Q_e, Q_i and the coupling coefficient between the two rings κ. These parameters were then used to construct simulation models that replicate the comb generation behavior of the physical chips. Based on this foundation, different parameter sweeps were performed to improve the understanding of their influence on the CE. These simulations led to an improved design for both 25 GHz and 50 GHz FSR configurations, achieving CE of 45% and 65%, respectively. The new designs were further analyzed in terms of their scalability with regard to input power, Q_i and FSR.

4.1 Chip Characterization of Existing Designs

As a starting point, multiple chips with FSRs of 25, 50 and 100 GHz were characterized, extracting their linear design parameters. These chips feature varying physical parameters, including the gap size between the bus waveguide and main ring, as well as the gap size between the main and auxiliary ring, which were swept across several values. From these chips, the following parameters were extracted from the transmission spectrum measurement: GVD, FSR, Q_e, Q_i. These parameters provide an overview of how the chip parameters vary when the physical sizes of the chip are adapted. This data is used for the next iteration of chip fabrication. For the chips used for comb generation, the coupling strength between the main and auxiliary ring κ was also measured. An overview of the measured parameters is provided in Appendix A.

Using two fabricated chips, with FSRs of 25 GHz and 100 GHz, frequency combs were generated to characterize the spectral comb shape and quantify their CE. The measured spectra were used to validate the simulation framework and to document the current experimentally achievable CE for both designs. Both combs have a sech-shaped comb and a line spacing corresponding to their FSR. Therefore, the comb with 25 GHz has 4× more comb lines within a set bandwidth compared to the 100 GHz design. At minimal input power, the measured chips reach CE of 6 % for 25 GHz and 51 % for 100 GHz FSR. These results demonstrate the significant

discrepancy between the designs in terms of current CE.

For the numerical simulation, we used the parameters extracted from the linear characterization measurements. The simulation input parameters are the following: FSR, GVD β_2, Q_e and Q_i from the main ring and the resonance split introduced by the auxiliary ring κ (Listed in the Appendix A). The quality factors of the auxiliary ring were not directly measured. Instead, we assumed a slightly decreased intrinsic Q of 6 million compared to the main ring. For the extrinsic Q, we used a similar value to that reported in [8], specifically 40 million. These assumptions are considered reasonable, as supporting simulations showed that the auxiliary ring's quality factors have negligible effects on the resulting comb.

Fig. 4.1 demonstrates good agreement between the measured and simulated spectra. The CE is predicted accurately by the simulations, but there is a difference in the final input power for the 100 GHz resonator. A detailed comparison of P_{in} and the resulting CE is provided in Tab. 4.1. This discrepancy can have various reasons. One possible explanation is that fibre-to-chip coupling losses might differ from the assumed values, meaning the losses are not distributed evenly between the input and the output facet. Another factor that might influence the P_{in} is a deviation in the extrinsic and intrinsic Q from the assumed values. The extrinsic Q decreases with increasing wavelength and the intrinsic Q is an average across all measured modes. The redshift of the measured comb shape compared to the simulation is Raman-induced and caused by the high soliton peak powers. Since this effect is not included in the simulation model, a small discrepancy arises between the measured and the simulated comb shape.

Table 4.1: Comparison of measurement and simulation data. P_{in} from simulation and measurement with resulting CE.

	FSR = 25 GHz		FSR = 100 GHz	
	Measured	Simulated	Measured	Simulated
P_{in} (mW)	19.95	19.95	10.47	7.50
CE (%)	6.34	5.57	51.08	50.84

4.2 Parameter Investigations

To gain a better understanding of photonic molecules, we investigated the impact of various parameters on the CE using the SP and CC codes. Starting with the chip parameter Q_e, which defines the coupling strength between the bus waveguide and main ring. Next, the influence of θ_c, the coupling strength between the two rings, was examined. The last chip parameter investigated is the size of the auxiliary ring.

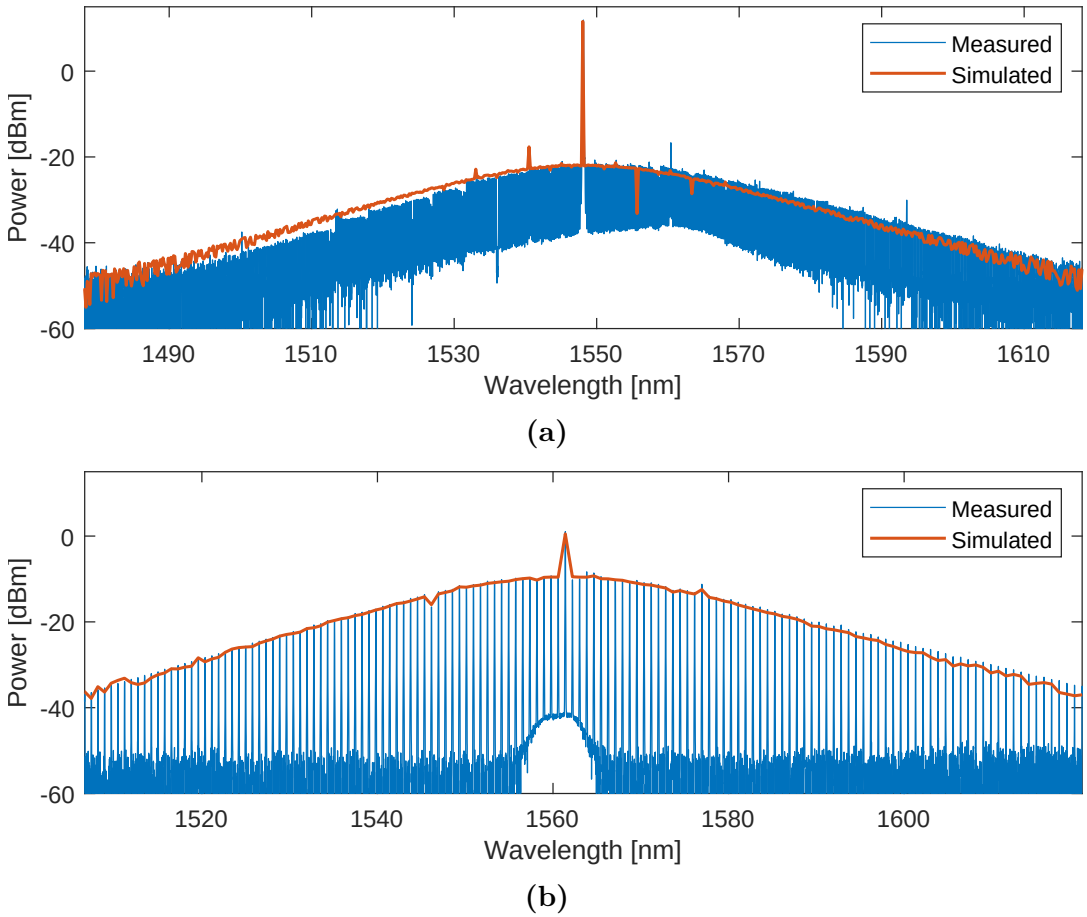

Figure 4.1: Measured comb spectra for **(a)** FSR = 25 GHz and **(b)** FSR = 100 GHz compared to simulation, using the characterized parameters from the linear chip measurement. To compensate for losses occurring after the chip in the laboratory setup, the measured spectra are normalized to the simulated comb line power. The resulting CE from the measurement are 6.3 % and 51.1 % for 25 GHz and 100 GHz, respectively.

4.2.1 Input Power and Extrinsic Q

One of the key parameters, which is usually defined before the design process, e.g., set by the application, is the input power, P_{in}. Accordingly, we begin by analyzing the effect of the input power on the CE. From theory, it is known that achieving a stable single soliton requires a balance between the nonlinear Kerr effect and the dispersion, as well as between gain and loss. This fundamental principle is described by the LLE (Eq. 2.18). Since the input power serves as the driver for generation parametric gain in our system and Q_{e} is the free parameter to adjust the losses α_{tot} from 2.8, there is a direct correlation between these two parameters. To maintain the balance of the soliton, the nonlinear phase shift introduced by $\gamma L|E|^2$, which is also dependent on P_{in}, must be compensated with a corresponding detuning value δ_0.

For the SP simulations, we performed a sweep over different values of Q_{e}, adjusting

the corresponding P_{in} and δ_0 for each point. The coupling coefficient κ was set to the maximum value at which a comb could still form. The maximal CE is reached close to the minimum input power at which the soliton can still be sustained. δ_0 has to be maximized to achieve the highest CE, as a higher δ_0 leads to a higher peak power and lower pulsewidth [23]. This narrow pulse in the time domain, in turn, corresponds to a broader comb spectrum with more comb lines. The SP simulation results, represented by the circles in Fig. 4.2, show the combinations of Q_{e} and P_{in} that yield maximal CE for these parameters. In the upper right region of the line formed by the simulation points, the optimal CE is not reached and can be improved by decreasing either P_{in} or Q_{e}. In the lower left region of the parameter space, where both Q_{e} and P_{in} are small, no soliton states are supported anymore. In addition, there is a point of maximal CE for one specific combination. For an FSR of 25 GHz this optimum occurs at $Q_{\text{e}} = 2$ million, with a corresponding P_{in} of 6.3 mW. As the FSR increases, this optimum shifts to lower Q_{e} values and higher P_{in}.

In the case of the CC simulations, which take into account the auxiliary ring, one more parameter must be considered. The coupling rate between the main and auxiliary ring κ. As a result of the coupling between the rings, avoided mode crossing occurs. Hence, the main and auxiliary resonances will be separated by κ for $\omega_{\text{res,main}} = \omega_{\text{res,aux}}$. To ensure that the laser couples into the resonance, the detuning per roundtrip is set to be $\delta_0 L = \frac{1}{2}\kappa/(2\pi\text{FSR})$. The CC simulations can predict the CE and comb shape with high accuracy, as demonstrated in Section 4.1.

The simulation results of the CC simulation show a similar behavior in terms of the correlation between Q_{e} and P_{in} compared to the SP simulations. As before, the points represent the combs with the lowest possible P_{in} and highest δ_0 for a given Q_{e}, resulting in a converged frequency comb with the highest achievable CE. However, the overall CE level obtained is lower. This reduction in CE can be explained by the losses introduced by the auxiliary ring, as seen from the perspective of the main ring. Because of the power distribution over both rings, the soliton loses power and the CE is diminished. Additionally, the simulations indicate that in the case of CC, the CE converges towards a constant value instead of reaching a distinct maximum. This trend becomes more visible in Fig. 4.3.

In Fig. 4.3 the CE is plotted over P_{in}, Q_{e} and θ_1. The comparison between the different parameters demonstrates that P_{in} and θ_1 follow the same trend, where there is a threshold P_{in} and θ_1 under which efficient DKS cannot be generated. This likely results from the low input power, which is not sufficient to introduce enough gain to the system, such that it can be balanced with a low power coupling factor θ_1. Above this threshold, the CE reaches a maximum and then appears to converge towards a stable value. Due to the inverse exponential relationship between Q_{e} and P_{in}, a narrow range of Q_{e} corresponds to a wide range of P_{in}. Consequently, this results in a significantly different CE trend when plotted over Q_{e}.

For the SP simulations, we also observe a cutoff Q_{e}, below which the CE drops significantly. This might be caused by elevated intracavity powers, which need to

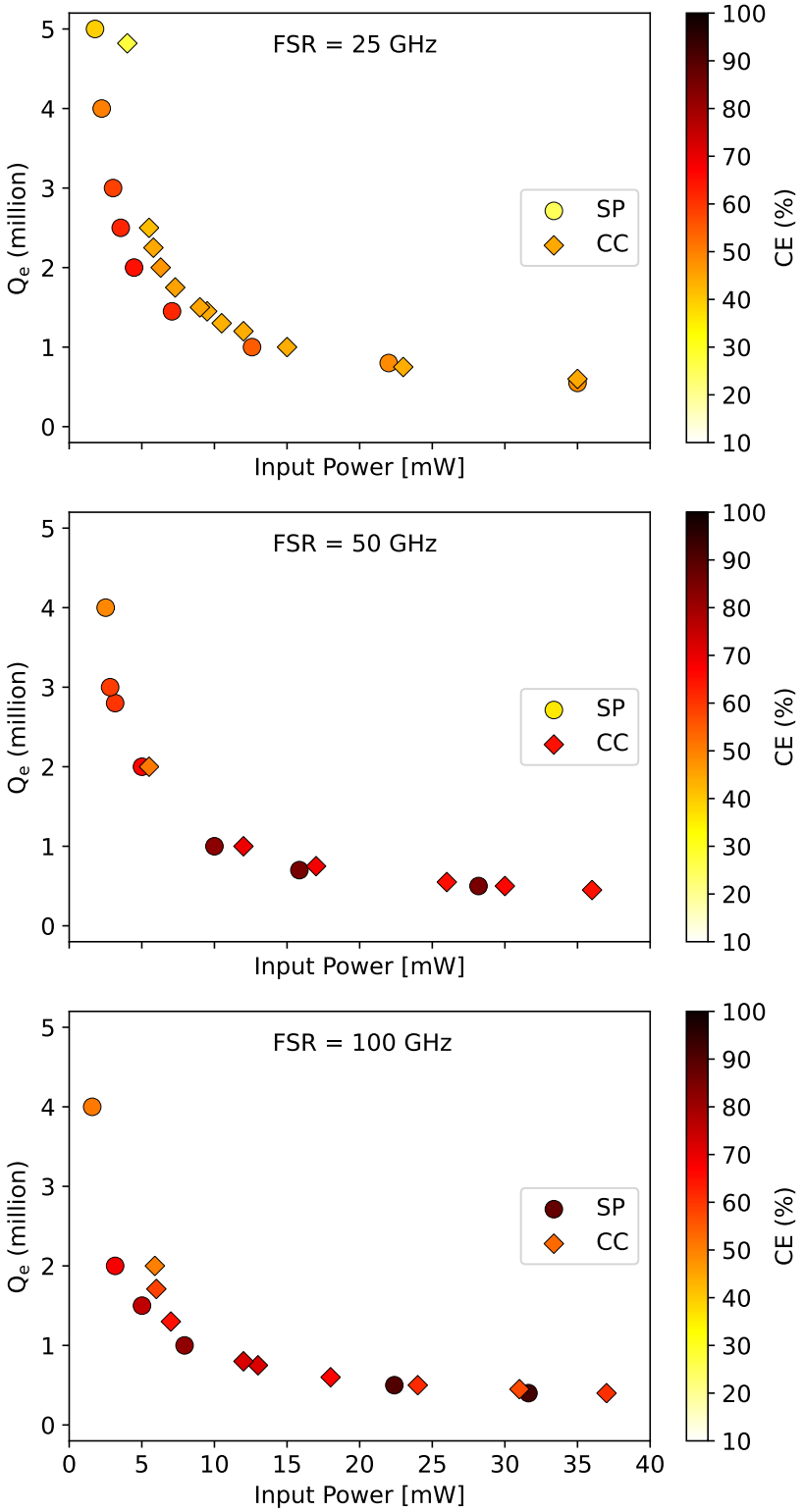

Figure 4.2: Comparison of simulation results from SP and CC simulations, presenting the correlation between Input Power and Q_e for different FSRs.

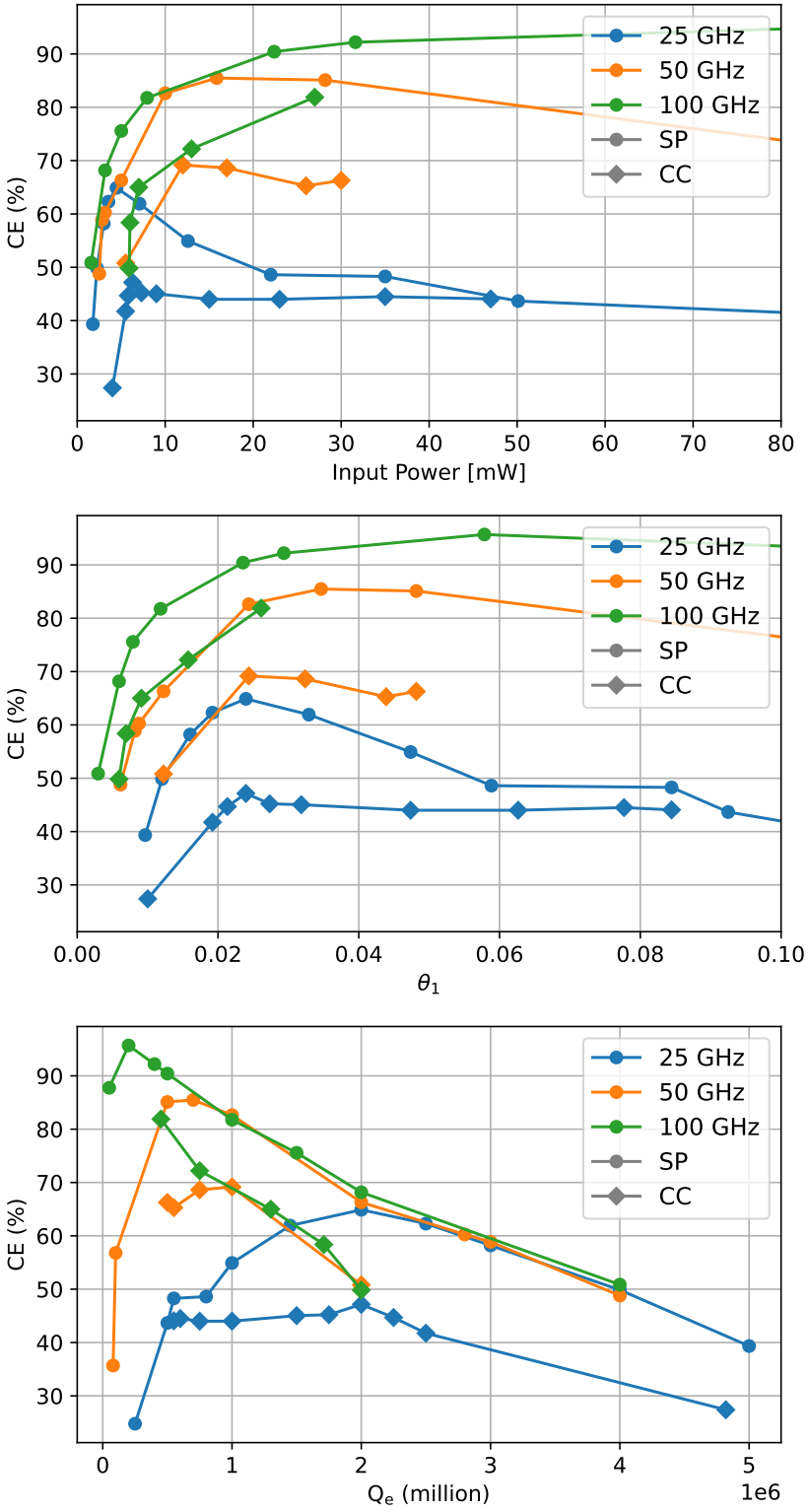

Figure 4.3: Comparison of simulation results from SP and CC simulations, presenting the trend of CE depending on P_{in}, θ_1 and Q_{e}.

be kept in balance with increasing detuning. However, it seems that at a certain detuning value, the comb cannot be sustained anymore in the SP simulations. Interestingly, for the CC simulations, especially for the 25 GHz design, we observe a constant CE value that the CC simulation converges to. If Q_e can be further reduced, the limit set by the SP simulations might be surpassed by using the photonic molecule layout. In that case, the range of high CE DKS would be expanded to even higher input powers, enabling wider comb spectra and higher power per line. However, decreasing Q_e requires higher input powers for gain generation, making the comb generation overall more challenging.

The figure also demonstrates that the cutoff or converged region of Q_e decreases with increasing FSR. One possible explanation is that lower intracity powers, resulting from larger cavity volumes, require lower coupling values to maintain the optimal balance between input power and coupling losses. Increasing coupling and input power further will only maintain the balance, but cannot improve the ratio of outcoupled comb power anymore. Higher FSR resonators, with lower cavity volume, can sustain high intracavity power at higher power coupling values, resulting in a different cutoff behavior.

4.2.2 Coupling Coefficient between the Rings

The second critical parameter identified in this thesis, which significantly influences the CE, is the coupling coefficient κ between the main and the auxiliary ring. To simplify the simulation process, we set the detuning to a fixed value that corresponds to half of the maximal resonance separation induced by the auxiliary ring, with

$$\delta_0 = 2\pi \frac{(f_{\text{res1}} - f_{\text{res1}})}{\text{FSR}} \ . \tag{4.1}$$

This ensures that the pump laser is always centered within the resonance. We simulated the 25 GHz photonic molecule at different Q_e and determined the corresponding maximum coupling coefficient and thus the highest detuning value. Fig. 4.4a presents an overview of the simulation results and demonstrates that with decreasing Q_e (increasing P_{in}), the maximal detuning value increases. Since the detuning is defined with Eq. 4.1, κ has to be increased as well. This effect arises from the increasing intracavity power with higher P_{in}, which leads to a stronger nonlinear effect and hence redshift of the cold resonance. To compensate for this stronger redshift, the detuning value must be increased.

Additionally, we investigated the CE when increasing the coupling coefficient at a fixed Q_e. Exemplary shown for a Q_e of 1 and 2 million in Fig. 4.4b and 4.4c. They show that with an increasing coupling coefficient, the ratio of mean power in the auxiliary ring relative to the main ring decreases. The ratio is defined as

$$\text{Ratio} = \frac{\overline{P}_{\text{aux}}}{\overline{P}_{\text{main}}} \ . \tag{4.2}$$

, where $\overline{P}$ denotes the mean power in the auxiliary and main ring, respectively. The decreasing power ratio results in a smaller percentage of the overall power residing

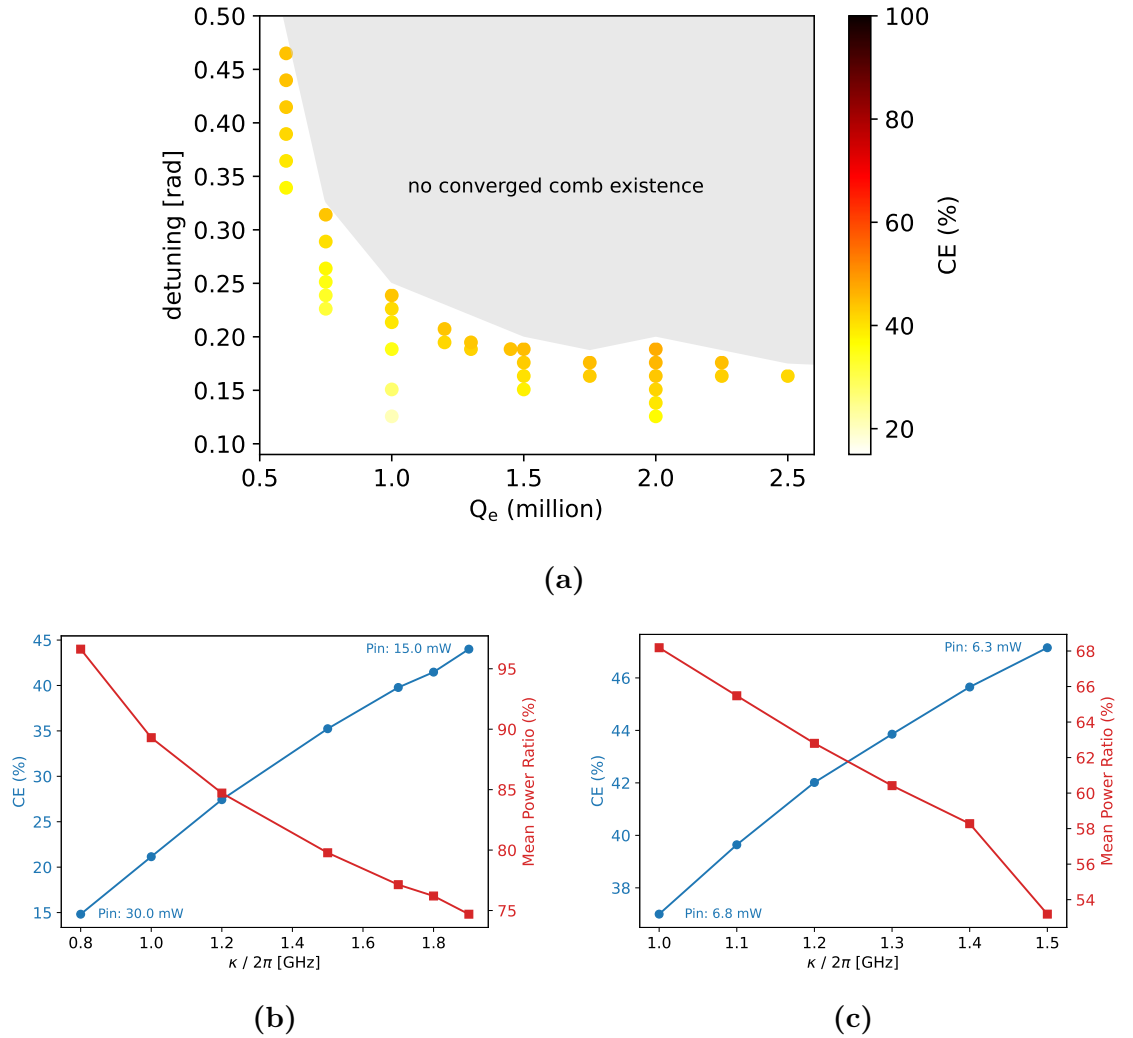

Figure 4.4: Simulation results of the CC code, when sweeping over different Q_e, detuning values and coupling coefficient, respectively, showing the corresponding conversion efficiency, (a) an overview over a wide parameter range. Specifically, Q_e of 1 million (b) and 2 million (c) were chosen to show the change in CE in reference to the power ratio between the auxiliary and main ring.

in the auxiliary ring, resulting in a higher peak soliton power in the main ring. Consequently, the CE of the resulting comb increases. Simultaneously, the required P_{in} to support the single soliton state decreases, since less energy is needed to achieve high soliton powers.

However, it is important to mention that there is a maximal coupling coefficient over which a DKS comb generation is not possible anymore. Additionally, it becomes more difficult to find a vector reaching the single soliton state. Therefore, it may be reasonable to leave a margin to the coupling coefficient used for a final design that goes into fabrication. This ensures a easier comb generation on the physical chip itself.

4.2.3 Auxiliary Ring FSR

An additional parameter investigated in this thesis is the FSR of the auxiliary ring. However, the accuracy of the model in capturing the influences of the auxiliary ring size is difficult to assess. The limitations of the model arise from the two-ring model with identical ring lengths, introduced in Section 3.3. While the number of modes is adjusted to match the actual size of the auxiliary ring, it is defined as an integer. Contrary, in practice, the ring size ratio is a non-integer to avoid strong mode coupling. Furthermore, the quality factors of the rings are kept constant when the ring FSR is varied.
From the comparison between simulation and measurements, it becomes evident that mode crossings can be predicted accurately for the 100 GHz design, but not for the 25 GHz design. Despite these difficulties, some initial trends can still be observed in the simulation results.

In general, it can be said that the ring size is a trade-off. While a high $\mathrm{FSR_{aux}}$ leads to lower losses and reduced power stored in the main ring, a low $\mathrm{FSR_{aux}}$ results in more mode crossings in the frequency domain. These mode crossings, in turn, enable more potential auxiliary ring resonances, which can be shifted into the main ring resonance for comb generation on the chip.
The selected design was simulated with varying ring size ratios M, keeping the decimal digits constant. These simulations showed that for both designs, changes in $\mathrm{FSR_{aux}}$ have minimal influence on the CE. For the 25 GHz design a change from $\mathrm{M} = 9.51$ to $\mathrm{M} = 6.51$ leads to a CE change of $< 1\%$. However, the simulations indicate that higher κ and δ_0 values can be achieved with higher $\mathrm{FSR_{aux}}$. Likely due to a higher proportion of the power remaining in the main ring, enabling higher detuning values. For the 100 GHz design, the $\mathrm{FSR_{aux}}$ had to be increased for high P_{in} designs to reach high CE and detuning values that correspond to those found in the SP simulations.

4.3 Presentation of new 25 GHz Design

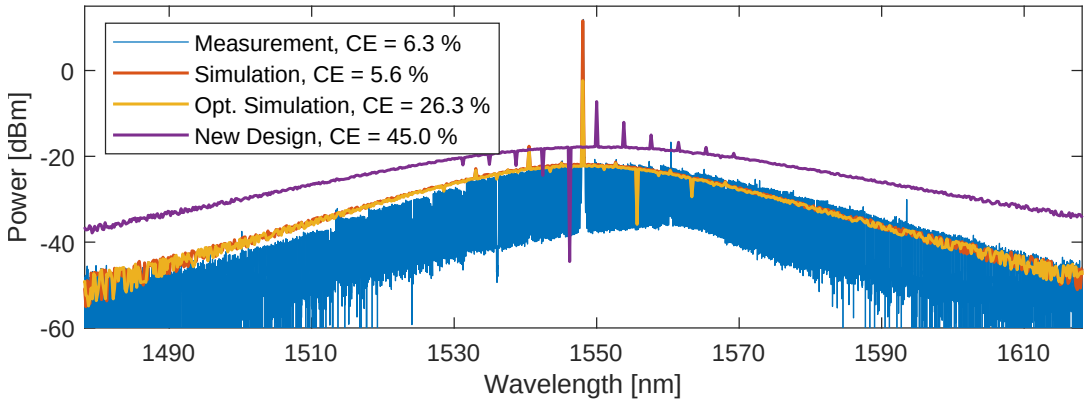

Figure 4.5: Comparison of comb spectra from the previous 25 GHz design from measurements and simulation to the new layout designed for $P_{\mathrm{in}} = 9\,\mathrm{mW}$.

Based on the parameter investigations, a new 25 GHz design was developed, which will be manufactured in the next fabrication cycle. The design is optimized for an input power of 9 mW, which is a feasible value for integrated lasers. To achieve maximum CE at $P_{\text{in}} = 9\,\text{mW}$, the Q_{e} from the original chip design was reduced to 1.5 million. The coupling factor corresponding to the maximum detuning value is $\kappa/2\pi = 1.5\,\text{GHz}$. Additionally, the FSR ratio $\text{FSR}_{\text{aux}}/\text{FSR}_{\text{main}}$ was increased to 9.51. With these parameters, a CE of up to 45% was achieved in the simulations. In the comb spectrum, the power per line is increased and the comb shape flattened, as shown in Fig. 4.5.

It is important to note that in simulations, it was possible to reduce the P_{in} below the measurement value for the existing design, which already leads to an increased CE. However, compared to the maximum CE of 26.3% achieved in simulation with the previous design, the CE of the new design achieves a significant improvement, reaching 45% CE.

4.3.1 Input Power Scaling

For further investigation, the new design was also examined in terms of its power scaling abilities. Similar investigations were previously conducted in [8] for a 100 GHz design using SP simulations. In Fig. 4.6, the power scaling is demonstrated with results of the CC code. As expected and consistent with the previous results, the power per line increases with increasing input power. Additionally, the parameter scaling follows the same trend observed in the results of the 100 GHz design, where the bus-ring and ring-ring coupling must be increased to adapt to higher input powers.

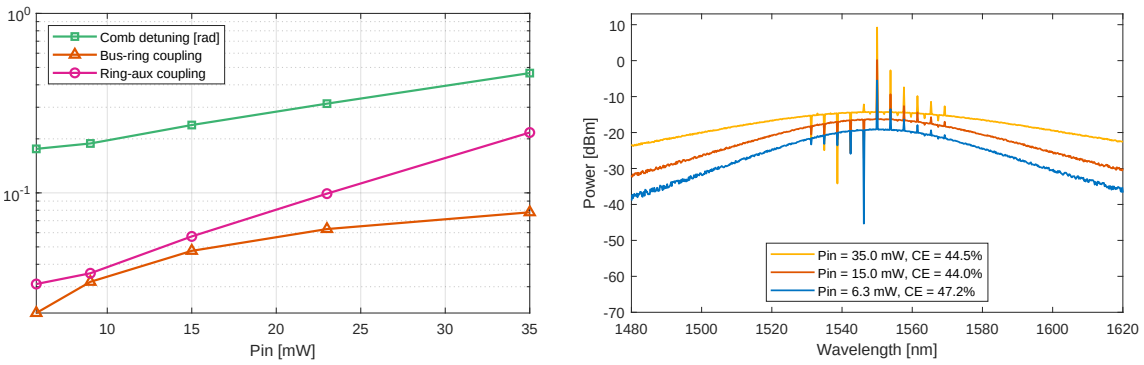

(a) **(b)**

Figure 4.6: (a) Scaling of parameters for changing input powers for the 25 GHz design and (b) the corresponding comb spectra with relative constant CE.

The results of the SP simulations exhibit a exponential trend for all parameters. In comparison to those results, deviation from this exponential trend can be seen in the low input power range for these new simulations. Those derivations might result from the fact that at low input powers below 5 mW we are below the threshold power

reaching the constant CE regime. Additional derivations can also be caused by the different simulation models that were used and the fact that the pump detuning was not considered in these simulations, since it was set to zero.

4.3.2 FSR Scaling

After designing a new high CE 25 GHz photonic molecule, we investigated how the designs scale with varying FSR. Therefore, designs with a FSR of 25, 50 and 100 GHz were compared at specific P_{in}. Fig. 4.7 shows the comparison at a P_{in} of 12 mW. This comparison introduces a parameter trend across FSRs, which can simplify the design process when adapting to arbitrary FSR values.

The comb spectra of the designs with 25 GHz and 50 GHz FSR exhibit similar comb shapes, differing primarily in the power per comb line. In contrast, the FSR = 100 GHz comb spectrum is more narrow. This indicates that a higher detuning and coupling between the rings can be achieved, resulting in a even higher CE and a comb shape more closely aligning with the other two designs. One possible explanation for the current limitation is that the auxiliary rings' FSR is too small, resulting in a decreased power level in the main ring.

Overall, the comb scaling demonstrates that, at a common input power, the achievable power per line for low FSR designs reduces. One strategy to counteract this effect is to reduce the intrinsic losses of the resonators, for example, by minimizing sidewall roughness. Simulations have demonstrated that an increased Q_{i} allows for a reduced input power while keeping the remaining parameters fixed. This, in turn, results in higher power per line at constant input power.

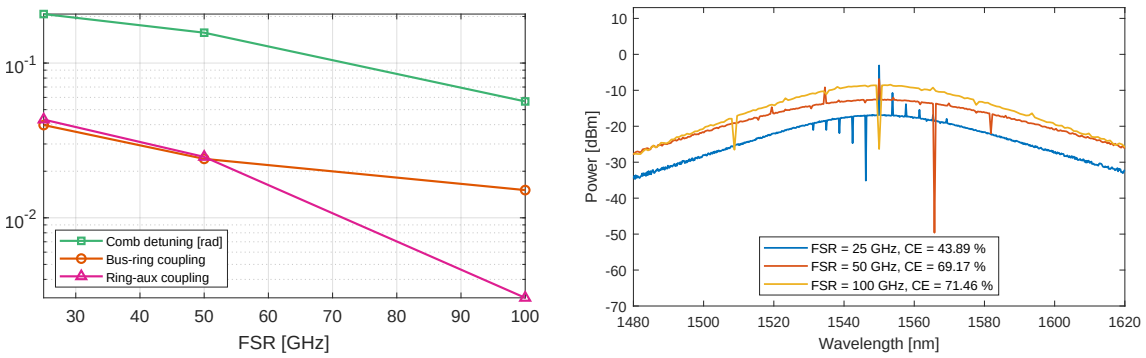

Figure 4.7: (a) Scaling of parameters for designs with FSR of 25, 50 and 100 GHz at a constant $P_{\text{in}} = 12$ mW and (b) the corresponding comb spectra.

5
Conclusion & Outlook

This chapter aims to reflect the work conducted during the thesis and summarize the key findings. We started with the characterization of existing chip layouts to define the current state of achievable CE for photonic molecule designs with different FSRs. To improve the CE for low-FSR photonic molecules, the extracted parameters from the measurements, along with extensive simulations, were used to define key parameters and their influence on the CE. The simulations were conducted on two models implemented in Matlab: the shifted pump and coupled cavity model. Both models are based on the Ikeda map and the Split-step Method. The chip parameters investigated include the coupling strength between the bus waveguide and main ring, as well as the coupling strength between the main and auxiliary ring. Additionally, simulation parameters like the input power and the detuning of the pump laser were analyzed with respect to their influence on the CE. Furthermore, initial investigations regarding the influence of the auxiliary ring size were conducted. Utilizing these findings, new designs with 25 GHz and 50 GHz FSR were developed and their input power scaling capabilities were examined. Combining all solutions, we derived general FSR scaling rules.

Using simulations, we demonstrated that Q_e exhibits an inverse power-law dependence on the input power. Hence, if a design has a target input power, the correct coupling strength between the bus waveguide and main ring must be chosen. This relation also depends on the FSR of the design. Given a constant input power, a higher Q_e must be chosen for low-FSR designs. Simulations investigating the coupling strength between the rings show that with increasing coupling, the power level in the auxiliary ring is reduced. This leads to a more favorable power distribution between the rings. The higher power in the main ring comes with a higher peak soliton power and, therefore, higher Kerr nonlinearity. This increased power, in turn, enables higher detuning values, which correspond to a higher CE due to the increased number of comb lines 4.4a. The detuning should always be chosen such that the pump laser is located in the red-detuned resonance. The simulation results also indicated that a smaller auxiliary ring further pushes the limit of maximum detuning in the photonic molecule system, enabling even broader comb spectra. These are essential to achieve flatter comb spectra, which are needed for communication applications and lead the path to octave-spanning low-FSR combs.

This thesis presents improved designs for 25 GHz reaching CE of 45% over a broad input power range in simulations. Additionally, a 50 GHz design reaching 65% was developed. Alongside these investigations, a universal design process was developed,

using the SP simulations to find an initial value combination of Q_e, P_{in} and detuning. These values can then be used to perform more detailed simulations in the CC code, allowing us to find the upper limit of the coupling strength between the rings and predict more accurate values for the comb shape and achievable CE.

The fabrication of the new design is currently in process. The chosen configuration is a 25 GHz device intended for operation at 10 mW input power. Future measurements of these chips will be used to verify the simulation results. Afterwards, the new designs could be used in a system-level application, e.g. a communication link, to demonstrate a proof of concept.

The simulations during this thesis also raised some further research questions. Most notably, the influence of the auxiliary ring size. For the 25 GHz simulations, the code cannot accurately predict the mode crossing influences on the comb shape as it does for 100 GHz devices. This indicates that the influence of the auxiliary ring is not fully captured in the model. We believe this originates from the simplified ring structure with identical ring lengths used in the code. Further research is necessary to investigate this aspect and potentially adapt the simulation model.

Bibliography

[1] B.-C. Yao, W.-T. Wang, Z.-D. Xie, Q. Zhou, T. Tan, H. Zhou, G.-C. Guo, S.-N. Zhu, N.-H. Zhu, and C. W. Wong, "Interdisciplinary advances in microcombs: bridging physics and information technology," *eLight*, vol. 4, p. 19, Oct. 2024.

[2] Z. Ye, F. Lei, K. Twayana, M. Girardi, P. A. Andrekson, and V. Torres-Company, "Integrated, Ultra-Compact High-Q Silicon Nitride Microresonators for Low-Repetition-Rate Soliton Microcombs," *Laser & Photonics Reviews*, vol. 16, no. 3, p. 2100147, 2022.

[3] S. A. Diddams, K. Vahala, and T. Udem, "Optical frequency combs: Coherently uniting the electromagnetic spectrum | Science," 2020.

[4] P. Trocha, M. Karpov, D. Ganin, M. H. P. Pfeiffer, A. Kordts, S. Wolf, J. Krockenberger, P. Marin-Palomo, C. Weimann, S. Randel, W. Freude, T. J. Kippenberg, and C. Koos, "Ultrafast optical ranging using microresonator soliton frequency combs," *Science*, Feb. 2018. Publisher: American Association for the Advancement of Science.

[5] B. Corcoran, M. Tan, X. Xu, A. Boes, J. Wu, T. G. Nguyen, S. T. Chu, B. E. Little, R. Morandotti, A. Mitchell, and D. J. Moss, "Ultra-dense optical data transmission over standard fibre with a single chip source," *Nature Communications*, vol. 11, p. 2568, May 2020. Publisher: Nature Publishing Group.

[6] D. T. Spencer, T. Drake, T. C. Briles, J. Stone, L. C. Sinclair, C. Fredrick, Q. Li, D. Westly, B. R. Ilic, A. Bluestone, N. Volet, T. Komljenovic, L. Chang, S. H. Lee, D. Y. Oh, M.-G. Suh, K. Y. Yang, M. H. P. Pfeiffer, T. J. Kippenberg, E. Norberg, L. Theogarajan, K. Vahala, N. R. Newbury, K. Srinivasan, J. E. Bowers, S. A. Diddams, and S. B. Papp, "An optical-frequency synthesizer using integrated photonics," *Nature*, vol. 557, pp. 81–85, May 2018. Publisher: Nature Publishing Group.

[7] M.-G. Suh, Q.-F. Yang, K. Y. Yang, X. Yi, and K. J. Vahala, "Microresonator soliton dual-comb spectroscopy," *Science*, vol. 354, pp. 600–603, Nov. 2016.

[8] B. Helgason, M. Girardi, Z. Ye, F. Lei, J. Schröder, and V. Torres-Company, "Surpassing the nonlinear conversion efficiency of soliton microcombs," *Nature Photonics*, vol. 17, pp. 992–999, Nov. 2023. Publisher: Nature Publishing Group.

[9] B. Helgason, F. R. Arteaga-Sierra, Z. Ye, K. Twayana, P. A. Andrekson, M. Karlsson, J. Schröder, and Victor Torres-Company, "Dissipative solitons in photonic molecules," *Nature Photonics*, vol. 15, pp. 305–310, Apr. 2021. Publisher: Nature Publishing Group.

[10] B. Helgason, *High-efficiency dissipative Kerr solitons in microresonators*. PhD thesis, Chalmers University of Technology, 2022.

[11] W. Bogaerts, P. De Heyn, T. Van Vaerenbergh, K. De Vos, S. Kumar Selvaraja, T. Claes, P. Dumon, P. Bienstman, D. Van Thourhout, and R. Baets, "Silicon microring resonators," *Laser & Photonics Reviews*, vol. 6, pp. 47–73, Jan. 2012.

[12] P. Rabiei, W. Steier, C. Zhang, and L. Dalton, "Polymer micro-ring filters and modulators," *Journal of Lightwave Technology*, vol. 20, pp. 1968–1975, Nov. 2002.

[13] C. R. Pollock and M. Lipson, *Integrated Photonics*. Boston, MA: Springer US, 2003.

[14] K. Twayana, *Advanced Characterization Techniques of Photonic Devices with Frequency Combs*. PhD thesis, Chalmers University of Technology, 2023. Chalmers University of Technology.

[15] V. Brasch, M. Geiselmann, T. Herr, G. Lihachev, M. H. P. Pfeiffer, M. L. Gorodetsky, and T. J. Kippenberg, "Photonic chip–based optical frequency comb using soliton Cherenkov radiation," *Science*, vol. 351, pp. 357–360, Jan. 2016. Publisher: American Association for the Advancement of Science.

[16] P. Grelu, ed., *Nonlinear optical cavity dynamics: from microresonators to fiber lasers*. Weinheim: Wiley-VCH Verlag GmbH & Co. KGaA, 2016.

[17] T. J. Kippenberg, A. L. Gaeta, M. Lipson, and M. L. Gorodetsky, "Dissipative Kerr solitons in optical microresonators," *Science*, vol. 361, p. eaan8083, Aug. 2018.

[18] T. Herr, V. Brasch, J. D. Jost, C. Y. Wang, N. M. Kondratiev, M. L. Gorodetsky, and T. J. Kippenberg, "Temporal solitons in optical microresonators," *Nature Photonics*, vol. 8, pp. 145–152, Feb. 2014. Publisher: Nature Publishing Group.

[19] G. P. Agrawal, ed., *Nonlinear fiber optics*. Optics and Photonics, Burlington: Elsevier Science, 5th ed ed., 2013.

[20] L. A. Lugiato and R. Lefever, "Spatial Dissipative Structures in Passive Optical Systems," *Physical Review Letters*, vol. 58, pp. 2209–2211, May 1987.

[21] S. Coen and M. Erkintalo, "Universal scaling laws of Kerr frequency combs," *Optics Letters*, vol. 38, p. 1790, June 2013.

[22] B. Helgason, M. Girardi, Z. Ye, F. Lei, J. Schröder, and V. T. Company, "Power-efficient soliton microcombs," 2022. Publisher: arXiv Version Number: 1.

[23] C. Bao, L. Zhang, A. Matsko, Y. Yan, Z. Zhao, G. Xie, A. M. Agarwal, L. C. Kimerling, J. Michel, L. Maleki, and A. E. Willner, "Nonlinear conversion efficiency in Kerr frequency comb generation," *Optics Letters*, vol. 39, p. 6126, Nov. 2014. Publisher: Optica Publishing Group.

[24] C. J. Krückel, A. Fülöp, T. Klintberg, J. Bengtsson, P. A. Andrekson, and V. Torres-Company, "Linear and nonlinear characterization of low-stress high-confinement silicon-rich nitride waveguides," *Optics Express*, vol. 23, p. 25827, Oct. 2015. Publisher: Optica Publishing Group.

[25] J. Liu, G. Huang, R. N. Wang, J. He, A. S. Raja, T. Liu, N. J. Engelsen, and T. J. Kippenberg, "High-yield, wafer-scale fabrication of ultralow-loss, dispersion-engineered silicon nitride photonic circuits," *Nature Communications*, vol. 12, p. 2236, Apr. 2021. Publisher: Nature Publishing Group.

[26] K. Twayana, Z. Ye, B. Helgason, K. Vijayan, M. Karlsson, and V. Torres-Company, "Frequency-comb-calibrated swept-wavelength interferometry," *Optics Express*, vol. 29, pp. 24363–24372, July 2021. Publisher: Optica Publishing Group.

A

Appendix

This appendix provides detailed information about the characterized devices from this thesis. Starting with Tab. A.1 listing all chip parameters used for simulations. Later, further plot give insights into the resonances, which were most likely used for the comb generation. This match is done, only comparing the measured wavelength in the comb generation with the resonances of the transmission spectrum. Additionally, the plots from the dispersion and quality factor characterization are provided.

Table A.1: Parameters for 25 GHz and 100 GHz FSR configurations, which where used for the comb simulations.

Parameters\Layout	100 GHz	25 GHz
FSR main (GHz)	99.69	24.96
FSR aux (GHz)	99.69	24.96
GVD β_2 (ps^2/km)	−91.1	−77.5
Q_i (million)	11.3	10.5
Q_e (million)	1.3	4.82
$\kappa/2\pi$ (GHz)	1.2	0.9

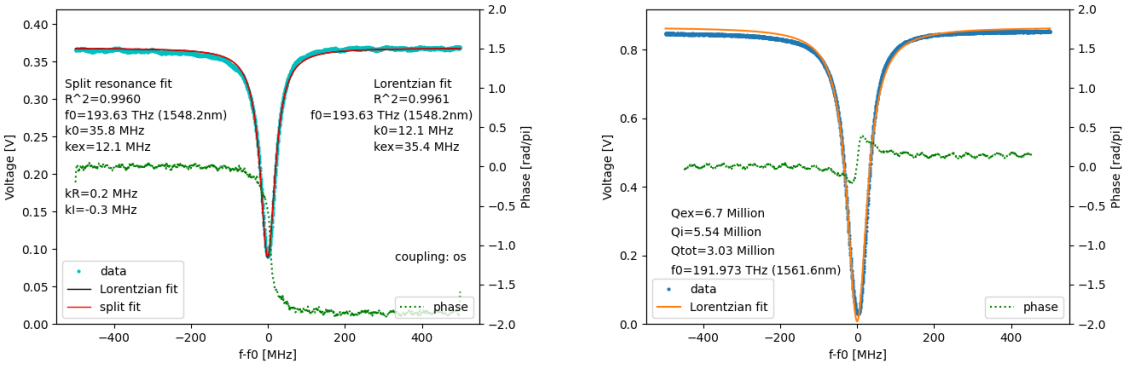

(a) **(b)**

Figure A.1: Measured resonances of the (a) 25 GHz and (b) 100 GHz devices used for the comb generation in this thesis.

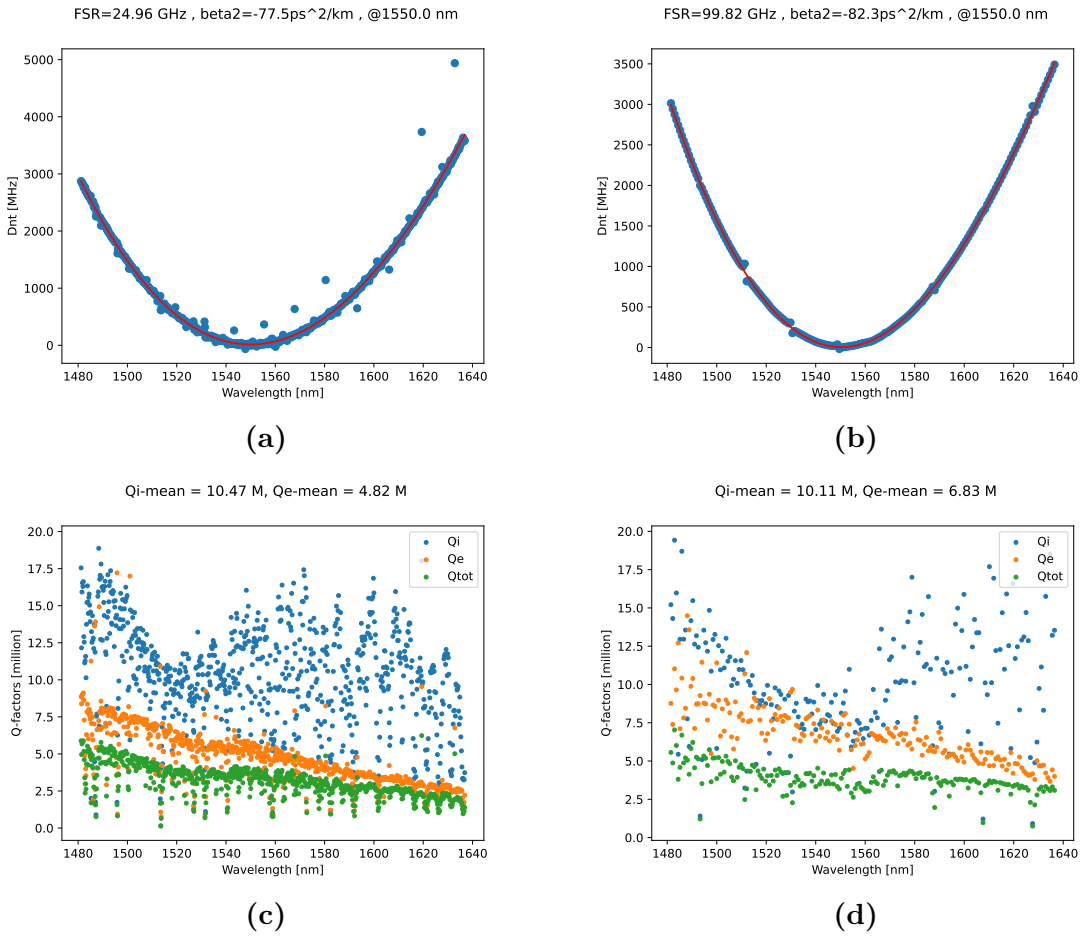

Figure A.2: Dispersion and quality factor development over the measured spectrum of the (a,c) 25 GHz and (b,d) 100 GHz devices. Providing detail insights into the GVD of the chip and the quality factor at the resonance used for the comb generation.

DEPARTMENT OF SOME SUBJECT OR TECHNOLOGY
CHALMERS UNIVERSITY OF TECHNOLOGY
Gothenburg, Sweden
www.chalmers.se

CHALMERS
UNIVERSITY OF TECHNOLOGY